Research Square

Preprints are preliminary reports that have not undergone peer review.
They should not be considered conclusive, used to inform clinical practice,
or referenced by the media as validated information.

Simultaneous sPIV and PLIF characterization of diverse airborne odor plumes

Elle Stark
University of Colorado Boulder
Aaron True
aaron.true@colorado.edu

University of Colorado Boulder
John P. Crimaldi
University of Colorado Boulder

Research Article

Keywords: particle image velocimetry, laser-induced fluorescence, gaseous plumes, turbulent dispersion, scalar transport

Posted Date: November 12th, 2026

DOI: https://doi.org/10.21203/rs.3.rs-10165984/v1

License: This work is licensed under a Creative Commons Attribution 4.0 International License.
Read Full License

Additional Declarations: No competing interests reported.

Simultaneous sPIV and PLIF characterization of diverse airborne odor plumes

Elle Stark[1], Aaron True[1*], John P. Crimaldi[1]

[1*]Civil, Environmental, and Architectural Engineering, University of Colorado Boulder, 4001 Discovery Drive, Boulder, 80303, CO, USA.

*Corresponding author(s). E-mail(s): aaron.true@colorado.edu;
Contributing authors: elle.stark@colorado.edu; crimaldi@colorado.edu;

Abstract

Many animals must navigate airborne odor plumes for successful foraging, mating, and habitat selection, but such navigation presents a challenging task due in part to chaotic transport of the odor through turbulent air. Despite broad ecological, industrial, and environmental importance, experimental investigation of such plumes remains limited, due largely to significant technical challenges associated with acquiring gaseous plume measurements at sufficient spatiotemporal resolutions. Here, we use simultaneous stereo particle image velocimetry and planar laser-induced fluorescence to jointly measure time-resolved velocity and scalar concentration fields for airborne odors transported by low Reynolds number grid turbulence in a recirculating wind tunnel. We introduce six datasets, including a baseline case (isokinetic, freestream release with neutral buoyancy) and five cases with perturbations to the source configuration (size, mass flow rate, buoyancy, bed proximity) or flow configuration (turbulence grid geometry). For each case, we present representative instantaneous flow and odor fields along with select statistical properties, highlighting Gaussian mean plumes, single-point concentration PDFs well-characterized by one-parameter Gamma distributions, and turbulence intensities that exhibit a combination of grid turbulence and a wake structure from the source tube. Finally, we leverage the multimodal data to compute turbulent odor fluxes and illustrate the connection between the velocity-derived finite-time Lyapunov exponent field and evolving structures in the odor field. These high-resolution measurements provide a rich suite of experimental data for use in fundamental studies of plume dispersion, olfactory neuroscience, and odor navigation in the data-scarce regime of low Schmidt number, low Reynolds number scalar transport.

Keywords: particle image velocimetry, laser-induced fluorescence, gaseous plumes, turbulent dispersion, scalar transport

1 Introduction

Passive scalar plumes transported by turbulent flows exhibit intricate dynamics in the co-evolution of their scalar and velocity fields. Such dynamics play a critical role in numerous environmental and engineering applications of interest, from dispersion of pollutants in the atmosphere (Cassiani et al. 2020) to indoor contaminant transport and mixing (Tung et al. 2009) to mixing in industrial processes (Speetjens et al. 2021). Of particular ecological importance is the transport and mixing of odors; animals perform impressive feats of navigation through such plumes to locate crucial odor sources like food and mates (Murlis et al. 1992; Steele et al. 2023). However, there is a lack of experimental datasets that quantify the dynamics of spatially distributed flow and odor data in such plumes, due largely to the experimental challenges of obtaining such measurements in gaseous conditions. In the current work, we seek to inform olfaction research, along with plume dispersion research more broadly, by providing high-resolution measurements, resolved in time, for both instantaneous and statistical characterizations of the simultaneous concentration and velocity fields from localized odor sources released into turbulent air.

Olfaction represents the least understood sensing modality, in part due to the turbulent transport process that transforms the odor signal as it travels from the source to the sensing animal (Celani et al. 2014). In certain respects the process benefits navigating animals, enabling odors to travel much farther and faster than diffusion alone, but along the way packets of odor are stretched, folded, and broken up into an intermittent signal that presents challenges for predicting the source location (Reddy et al. 2022). In such plumes, convergence of concentration statistics like the mean plume typically takes longer than the behavioral timescales relevant to olfactory navigation (Liao and Cowen 2002), so animals cannot use smooth gradients from such statistical properties to navigate to the source. Instead, many navigating organisms sense and leverage high-speed information from the fluctuating plume (Moore and Atema 1991; Ackels et al. 2021; Szyszka et al. 2014). The recognition of olfaction as a *fast* sense underscores the importance of obtaining high-frequency data throughout the plume envelope to understand the signals available to animals during the search process (Crimaldi et al. 2022).

Despite the ecological importance of fast odor plume dynamics, there is a lack of spatially distributed, time-resolved experimental data for airborne plumes, due largely to the experimental challenges involved. Historically, research on dispersion of airborne odors typically relied on single-point measurements with high time-resolution, including field studies of odor plume structure under varied environmental conditions (Murlis et al. 2000) and laboratory studies probing specific aspects of scalar release and flow conditions (Justus et al. 2002). Studies with spatially distributed measurements of evolving odor plumes have generally been confined to aqueous conditions (Webster and Weissburg 2001; Crimaldi and Koseff 2001; Liao and Cowen 2002; Crimaldi 2008), and while it is possible to match the Reynolds number (ratio of inertial to viscous effects) of an airborne plume in aqueous experiments, the Schmidt number (ratio of momentum diffusivity of the fluid to molecular diffusivity of the scalar) cannot be matched at the same time (Connor et al. 2018). This inability to fully match airborne

conditions in water makes it necessary to perform experiments in gaseous conditions to obtain data for airborne plumes.

To address the lack of data in airborne conditions, Connor et al. (2018) gathered the first spatially distributed datasets specifically configured to mimic naturalistic gaseous odor plumes. Compared to large-scale atmospheric dispersion cases, key configuration differences include the larger relative source size (i.e., source to integral size ratio) and low Reynolds number conditions, with the relevant scales of fluctuations generated from obstacle wakes rather than turbulent boundary layer formation when the odor is released far enough from a local boundary. Using this olfaction-targeted configuration, Connor et al. (2018) measured concentration data for three plume cases using planar laser-induced fluorescence (PLIF). The resulting datasets have been utilized extensively for applications including laboratory protocols for olfactory stimuli (Álvarez Salvado et al. 2018; Kathman et al. 2024; Gumaste et al. 2020), developing and testing navigational algorithms and information theoretic explanations for animal search behavior (Hengenius et al. 2021; Boie et al. 2018; Victor et al. 2019), and as evidence for trends in the statistical properties of odor plumes under various conditions (Reddy et al. 2022; Siliciano et al. 2025).

In recent years, however, mounting evidence in olfaction research reveals that navigating animals leverage not only the odor signal from the concentration field, but also mechanical cues from the velocity field in their search behaviors (Dürr et al. 2022). Evidence for such *multimodal* navigation has been found in bees (Tiraboschi et al. 2021), fruit flies (Suver et al. 2023; Stupski and Van Breugel 2024), moths (Tuckman et al. 2021), and various arthropods (Steele et al. 2023). At the neural processing level, researchers have demonstrated the integration of both mechanosensory and chemosensory signals in the brain during olfactory navigation (Patel et al. 2022). This integration of both wind and odor information for behavioral responses motivates the need to directly measure velocity fields along with the concentration fields in naturalistic plumes, with spatial and temporal resolution relevant to an organisms' sensory architecture.

To that end, the current work implements simultaneous stereo particle image velocimetry (sPIV) and acetone PLIF for the concurrent measurement of three-component velocity fields and concentration fields, respectively, in the plane of measurement. Since the 1990s, researchers have combined PIV and PLIF techniques for flow and scalar measurements in various applications (Frank et al. 1999; Simoens and Ayrault 1994). Combustion and fuel mixing research, for example, extensively applies joint PIV/PLIF techniques, but such applications exhibit markedly different characteristics than odor transport and mixing (Tanahashi et al. 2005; Filatyev et al. 2007; Petersson et al. 2007; Sadanandan et al. 2008; Coriton et al. 2014; Sharaborin et al. 2021). Studies that combine PIV and PLIF in the context of plume dispersion remain less common, despite the fundamental role of turbulent mixing in the evolution of the scalar field. A few experimental studies achieved time-resolved flow and scalar data to investigate passive scalar transport, but did so in aqueous conditions for experimental tractability (Liao and Cowen 2002; Reijtenbagh et al. 2021; Lim and Vanderwel 2023; Young et al. 2022). In gaseous plume contexts, studies generally focus on high-Re conditions, rendering time-resolved measurements impractical. Recently,

for example, Wall and Pathikonda (2025) measured spatially distributed simultaneous PIV/PLIF for the case of a very small source released into a turbulent boundary layer, a configuration that precluded time-resolved measurements.

By contrast, the current work measures time-resolved velocity and concentration data for airborne odor plumes in low-speed wind tunnel grid turbulence. We collected the datasets at a temporal resolution of 20 Hz, yielding time-resolved data in a plume dynamics sense, that is, we see smooth frame-to-frame evolution of turbulent structures at this frequency. A sampling frequency of 20 Hz has also been identified as a minimum sampling rate for accurate distance estimation in outdoor naturalistic plumes (Nag and Van Breugel 2024). In terms of spatial resolution, the experimental setup allows us to resolve length scales smaller than the Kolmogorov and Batchelor scales for the velocity and concentration fields, respectively. To provide data and statistical analysis for a range of naturalistic conditions, we vary key parameters across the collected datasets.

Along with filling a critical data gap in multi-modal olfactory navigation research, these datasets advance experimental capabilities and provide a cohesive suite of data for researching a relatively under-studied regime in plume dispersion literature: turbulent mixing in low Reynolds number, low Schmidt number conditions (e.g., diffusive/gaseous contexts). While these regimes have been simulated numerically, there are many open questions as to the spectral characteristics of concentration fluctuations around the dissipation scale, which require experimental investigation (Sreenivasan 2019). To our knowledge, these may be the only direct experimental measurements of simultaneous velocity and concentration fields for passive scalars that resolve these small scales. The time-resolved, dual modality datasets also enable the application of modern Lagrangian methods for plume dispersion research, such as the application of Lagrangian Coherent Structures to investigate the relationship between structures in the flow field and transport of scalars (Haller 2014).

2 Experimental Methods

2.1 Facility overview

We measured the odor plume data in a low-speed wind tunnel with height 2.8 m, width 1.4 m, and depth 0.25 m (Fig. 1A). The wind tunnel is a vertical recirculating system driven by a variable speed axial fan with closed-loop wind speed control (using a pressure drop measurement through an integrated circular orifice). The tunnel, manufactured by Smart Blade, was designed for wind speeds ranging from 0.1 to 1 m/s, and calibrated by the manufacturer using laser Doppler anemometry at the center of the test section. We performed additional calibration, detailed in Appendix A, to fine-tune the controller settings for each wind speed. Flow was conditioned using a honeycomb panel, then a turbulence grid generated fluctuations upstream of the test section that decay in the downstream direction. The test section is 50 cm wide x 25 cm tall x 100 cm along the flow direction, with a glass window (x-y plane) on one side for imaging and a narrow slit with a quartz window (y-z plane) for low-attenuation transmission of the laser sheets (specifically the UV laser sheets used for PLIF excitation). Prior to data acquisition, PIV particles (DEHS aerosolized using a LaVision

GmbH aerosol generator with Laskin nozzle to generate sub-micrometer particles) were injected into the wind tunnel until the desired seeding density was reached. For the PLIF tracer, we saturated a carrier gas (air and helium blend which can be tuned with integrated mass flow controllers to prescribe source buoyancy) with acetone vapor by flowing the gas through a copper tube with diameter 5 cm and length 155 cm, partially filled with liquid acetone (Fig. 1B). The long residence time of the tube and high-thermal conductivity copper walls ensure full acetone vapor saturation of the carrier gas and mitigation of evaporative cooling effects. Collectively this ensured a constant acetone vapor source concentration introduced to the test section, since the headspace concentration depends on the saturation vapor pressure of acetone which is highly temperature dependent (see Appendix B for thermal testing of our system that showed a highly stable temperature). The acetone mixture was released from a round tube centered cross-stream at the upstream end of the test section. To seed the plume source itself for PIV measurements within the plume envelope, additional DEHS aersols were collected in a seeding reservoir, then a mass flow controller sent a small rate of air into the tubing upstream of the source, which was blended evenly with the saturated carrier gas using an-inline helical mixer. After collecting each dataset, we vented the wind tunnel to replace the existing air with clean ambient air prior to initiating another plume, so that the background conditions and seeding densities were consistent across datasets. We also used an integrated activated charcoal filter to mitigate rising background acetone levels, thereby maximizing SNR of the plume measurements.

2.2 Data acquisition: planar laser-induced fluorescence

We used PLIF to measure the odor concentration field with acetone used as an odor surrogate. Acetone vapor exhibits fluorescence intensity that is linear with partial pressure and with excitation energy across a wide range of partial pressures and energy levels, allowing for quantitative concentration measurements based on imaged intensity values (Lozano et al. 1992). For exciting acetone fluorescence, a dual-head Nd:YAG 1064 nm laser (Lumibird QSmart Twins 850), equipped with a 4th harmonic generator crystal, produced 266 nm pulses at a frequency of 10 Hz per head and approximately 100 mJ/pulse. The heads were staggered in time to yield 20 Hz imaging resolution at 100 mJ/pulse excitation per image. UV energy output through Nd:YAG harmonic generation depends strongly on the temperature and orientation of the harmonic generator crystals. Regular laser system tuning and pulse energy measurements were required to maintain system performance, ensure consistent fluorescence excitation energies, and reduce head-specific variations in laser energy. Details on the tuning procedures and resulting energy levels are provided in Appendix C. Cylindrical UV sheet optics (TSI Inc.) transformed the beam into a thin light sheet (sheet waist thickness approximately 1 mm) parallel with the test section floor, centered on the acetone output tube.

We imaged fluorescence from the acetone plume using a Zyla ZL41 Cell 5.5 MP sCMOS camera (monochrome, 16-bit, 2160×2560 native resolution with 2×2 hardware binning for 1080×1280 raw images), selected for its low readout noise and true global shutter, paired with high dynamic range and high quantum efficiency (about 45% to 60% in the range 440 nm to 500 nm, which shows highest power in the acetone

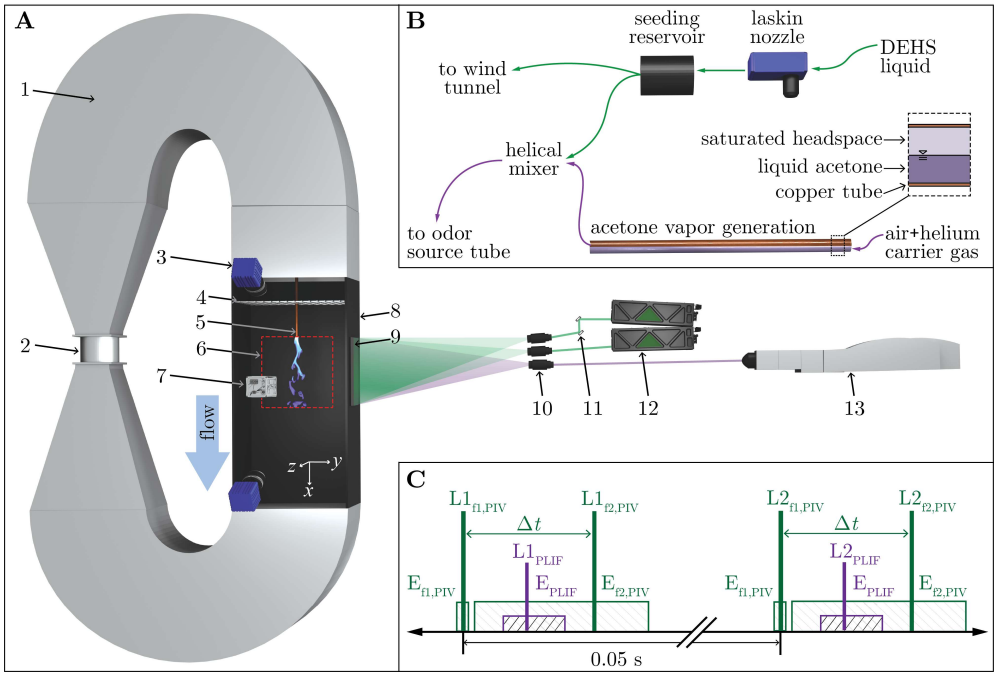


Fig. 1 Experimental schematic showing (A) wind tunnel, illumination, and imaging setup, (B) acetone generation and DEHS seeding apparatus, and (C) timing diagram for 20 Hz synchronized data showing laser pulses, L, and exposure times, E, for frames f1 and f2, with PIV-related quantities in green and PLIF-related quantities in purple. Details: 1) vertical low-speed wind tunnel, 2) axial fan 3) two PIV sCMOS cameras 4) turbulence grid, 5) odor source tube 6) 30 cm square field of view, 7) PLIF camera, 8) test section, 9) quartz window, 10) sheet optics, 11) mirrors, 12) PIV lasers, and 13) PLIF lasers.

fluorescence spectrum). We minimized external light sources and removed background acetone with an activated charcoal filter in the tunnel to help boost the signal-to-noise ratio, and fit the camera with a 532 nm notch filter to avoid crosstalk with any stray 532 nm light from the PIV system. The experimental configuration allowed us to resolve an approximately 30 cm square field of view with about 0.3 mm/px resolution.

2.3 Data acquisition: stereo particle image velocimetry

Stereo PIV (sPIV) quantifies three components of the velocity field in a plane (2D3C) using two oblique cameras to resolve out-of-plane motion along with the in-plane velocity components (Prasad 2000). We seeded the tunnel and plume with dispersed DEHS aerosols (mean diameter approximately 1 micron). These aerosols have low Stokes number, ensuring they behave as passive tracers. We then imaged the Mie scattering in a sideways configuration. Two double-pulse Nd:YAG 532 nm lasers (Quantel EverGreen model EVG00200) each emitted paired pulses at a frequency of 10 Hz and energy of about 200 mJ per pulse, such that by alternating the lasers we achieved 20 Hz temporal resolution. Cylindrical sheet optics (LaVision GmbH) transformed the

beams into thin light sheets (estimated sheet waist thickness of 1.5 mm) aligned with the UV light sheets generated for the PLIF imaging.

Two LaVision GmbH Imager sCMOS cameras (monochrome, 16-bit, 2560×2160 resolution) collected image pairs of the particles. The cameras were positioned 75 cm from the test section and 80 cm apart from one another, centered on the desired field of view (using the 30 cm × 30 cm calibration plate as a target) and angled such that their fields of view completely overlapped. They were positioned obliquely to the FOV at angles between 25° and 26° from perpendicular relative to the plane of the calibration plate, resulting in an angle between the optical axes of the cameras of 50°to 52°. This angle of about 50° between the cameras balances the random error in the z (out-of-plane) velocity component (which decreases with decreasing angle toward the test section) with random error in the x and y (in-plane) velocity components (which increases with decreasing angle toward the test section) (Smith and Neal 2016). Schiempflug adapters on the cameras adjusted the focal plane to minimize focus issues arising due to the oblique viewing angle. The PIV cameras were fitted with 532 nm bandpass filters to block any stray light from acetone fluorescence. The time between each image in an image pair, Δt, is a critical consideration for the quality of the PIV results. We computed the time delay, Δt between image pairs such that at the average flow velocity, a particle moves about 1/4 of the way through the estimated smallest potential interrogation window:

$$\Delta t = \frac{N}{4M\overline{u}} \tag{1}$$

where N is the size of the interrogation window (conservatively estimated as 12 px for these experiments), M is the magnification, and $\overline{u}$ is the average flow velocity. We also ensured sufficient seeding density to allow for resolving small-scale velocity fluctuations without particle overlap decreasing the correlation quality, with densities ranging from around 0.015 to 0.25 particles per pixel, yielding approximately 8-14 particles per 24 × 24 pixel interrogation window.

2.4 Timing and control

A timing diagram for synchronizing the data acquisition from both modalities is shown in Fig. 1C. To achieve this timing, two instances of DaVis were used that each controlled a separate programmable timing unit (PTU): one for triggering the cameras and one for triggering lasers. Camera triggering required a 20 Hz imaging rate, controlled by one DaVis instance. The lasers, however, required a 10 Hz triggering rate, because we alternated firing separate laser heads at a 10 Hz rate in order to achieve 20 Hz illumination. Due to both software limitations (DaVis did not allow trigger rates lower than image rates at the time of the study) and harware limitations (the limited number of connections from each PTU), we used a separate DaVis instance and PTU for sending the laser flashlamp triggers versus the camera triggers. The two PTUs were synchronized with a signal generator sending a 20 Hz signal to the PTU controlling the cameras and a 10 Hz signal to the PTU controlling the lasers. The timing setting in DaVis was set to 'External cyclic' to set timing based on this signal, and the reference time for both instances to 10,000 μs to ensure synchronization of the illumination and imaging systems. The stereo PIV images obtained by the two Imager

sCMOS cameras were recorded in the DaVis instance that controlled the camera triggers. The PLIF images obtained by the Zyla sCMOS camera, however, were recorded by a separate image acquisition software: Andor Solis 4.32.

PC control was also implemented for operation of the mass flow controllers (MFCs) and high-level operation of the Q-smart Twins lasers. The MFCs were controlled using a LabView script designed to set each device to the desired flow rate in standard liters per minute (SLPM), computed via linear interpolation of the 0 to 5 V voltage range and 0 to 1 SLPM flow rate range. This control allowed fine tuning of both source buoyancy (carrier gas blends) and PIV aerosol seeding densities in the plume envelope. The Q-smart lasers were operated via Q-touch software, using the Ethernet connection option to the laser head power supply units (see the Q-smart 850 manual for details operation of the lasers using Q-touch).

2.5 Data processing: general

Converting from raw images to quantified data required image processing procedures specific to each data modality. The unique aspects of the processing for each modality are presented in the subsections below. Here, we describe the common aspects between the processing procedures. Namely, we alternated different double-pulse lasers for the PIV acquisition and different laser heads for the PLIF acquisition; therefore, both the velocity and the concentration fields required laser-specific processing to account for the unique characteristics of the light sheet energy level and energy distribution of each laser head, along with any slight differences in sheet alignment. This entailed processing data separately for alternating data time-steps, that is, processing two 10-Hz datasets that followed the same procedures, but yielded results that accounted for the unique features of each laser. The processed 10 Hz datasets for each laser were then interleaved to create one 20 Hz dataset for each modality.

The resulting velocity vector fields and scalar concentration fields contained data distributed across two different spatial grids. To allow for direct comparisons and computations across the two modalities, the PIV datasets were spatially interpolated onto the 0.3-mm native grid of the PLIF data (via linear interpolation implemented in Python with scipy.interpolate module). This yielded the results analyzed below: scalar concentration data and 3-component velocity data at 20 Hz temporal resolution for a 5 min duration, reported on a 0.3 mm grid over a 30 cm $\times$ 30 cm (cross-stream $\times$ streamwise) domain.

2.6 Data processing: planar laser-induced fluorescence

For PLIF processing, following Crimaldi (2008) and Connor et al. (2018), we computed normalized concentrations $\frac{C}{C_0}$ using

$$\frac{C}{C_0} = \frac{1}{a_c}\frac{I-b}{F-b} \tag{2}$$

where I are raw intensities, a_c is the normalization coefficient, b is the background image (acquired with the laser on but without any tracer present), and F is the flat-field image (acquired by filling the test section with a uniform and constant tracer

concentration with the light sheet on). We used LaVision GmbH DaVis 10.2.0 software to implement the algorithm via the following processing steps. First, we accounted for slightly rising background acetone in the recirculating wind tunnel by computing the linear rate of increasing intensities in each dataset for an area outside the plume envelope. We then created a set of background images by multiplying the average background image obtained prior to data collection (averaged across a set of 400 images) by the computed rise rate for each frame. Subtracting this background set removed the slightly rising acetone background fluorescence along with constant reflective surfaces, stray light, and the camera sensor's dark response. Next, dividing the data by the average of a series of flat-field images (averaged across a set of 400 background-subtracted images) accounted for spatial variations in the light sheet and non-uniformity in the collection optics (Van Cruyningen et al. 1990). Note that due to the staggering of laser head pulses in time to achieve 20 Hz resolution, PLIF image processing used head-specific background and flat-field images. This mitigated systematic errors due to differences in laser energy output and light sheet geometry. The normalization coefficient was determined by the instantaneous odor source intensity measured in a small area (about 10 mm^2) at the plume outlet. Then, we used one pass of 7×7 median smoothing to decrease noise in the image while preserving gradients in the concentration field. Lastly, geometrical camera distortions were corrected using images of a precisely machined calibration plate (LaVision GmbH, 309-15) and a pinhole calibration model, with a fit error of 0.14 to 0.16 px for these datasets. The processed concentration fields have a spatial resolution of 0.3 mm (Fig. 2).

2.7 Data processing: stereo PIV

For stereo PIV, the processing procedure involved image pre-processing, vector computations, and vector field post-processing. We used LaVision GmbH DaVis 10.2.0 software for data processing, including vector computations.

Raw images were pre-processed with the aim of removing the background from particle images and increasing particle contrast to remove bias and improve the fidelity of image pair correlations. To this end, we first subtracted the minimum pixel intensity over all time to lower background signal levels. Next, we used a min/max filtering process to homogenize particle intensities I, implemented in DaVis at each pixel as:

$$[I - \min(I_{\text{local}})]\frac{\max(I_{\text{region}})}{\max(I_{\text{local}})} \tag{3}$$

where the "local" and "region" subscripts refer to a local square window with user-defined side length ℓ, and a larger-region square window with sides length 10ℓ. We selected a window length of 8 pixels to balance homogenization of the particle intensities with avoiding the introduction of artificial larger-scale intensity distortions across the domain.

The vector computations used a multi-pass processing scheme using an initial pass with interrogation window size of 64 px and four passes at the final window size of 24 px, using adaptive window shapes with 75% overlap. During vector field computation, a pinhole calibration model was used to dewarp images in pixel space to real world

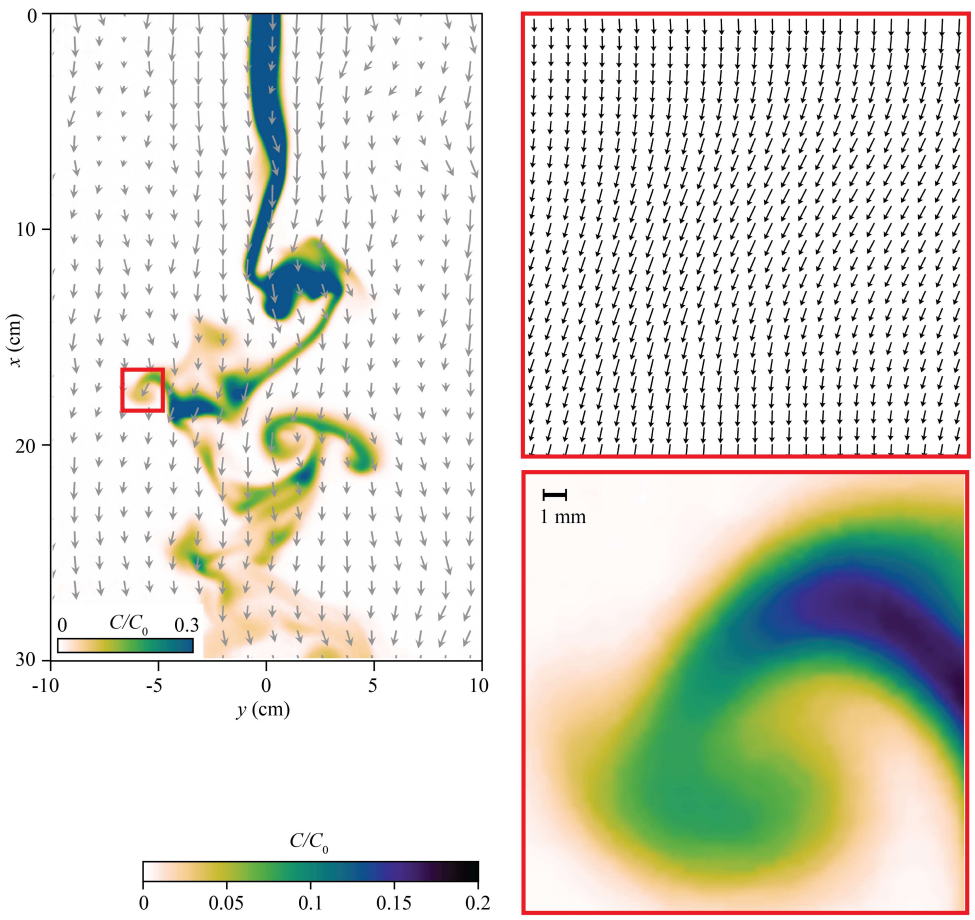


Fig. 2 Illustration of spatial resolution of sPIV and PLIF measurements. Left: example snapshot of instantaneous data for velocity and concentration fields across full domain, with 2×2 cm region of interest (ROI) outlined in red. Right: full-resolution measurements of velocity field (top) and concentration field (bottom) in ROI, showing sub-mm resolution of both fields.

space, which yielded fit errors of about 0.12 px and 0.15 px for the lower and upper cameras, respectively. The stereo self-calibration algorithm in the software additionally allowed for corrections to any misalignment of the calibration plane and image plane by creating a map of the image disparities and adjusting the images accordingly (Wieneke 2005), resulting in a stereo reconstruction error of approximately 0.13 mm for these datasets.

For vector validation, we removed spurious vectors that showed a peak ratio of less than 1.5 between the correlation value of the highest peak in the correlation matrix to the second-highest peak. Median filtering using a 5 × 5 filter window was then used for outlier detection and removal. Finally, post-processing of the vector fields involved interpolation of any missing vectors resulting from vector removal,

then anisotropic denoising to smooth the vector fields. The anisotropic denoising fit a polynomial function to the vector field to smooth gradients, but used the locally computed uncertainty values to limit the polynomial fit to adjust values only up to a maximum of the local uncertainty value. The processed vector fields had a spatial resolution of 0.75 mm (Fig. 2). For visualization and analysis of the PIV and PLIF data together, we interpolated the PIV vectors onto the native PLIF 0.3 mm grid to align with the concentration data.

2.8 Conditions tested

We collected datasets spanning a range of naturalistic airborne odor plumes with a diversity of spatiotemporal structure in the concentration and velocity fields. In the current work, we present six cases that systematically tested the effects of varying one plume configuration parameter in each case (Table 1). The *baseline* case is an isokinetic, neutrally buoyant release from a 1.25 cm inner diameter source tube in freestream conditions (i.e., the source is far enough from test section walls to avoid significant boundary layer effects), using a regular (square mesh) turbulence grid positioned 15 cm upstream of the source release, with 30 cm/s average wind speed. From this baseline, we changed one configuration parameter in each additional case as summarized below. Non-dimensional parameters characterizing these changes are listed in Table 1.

For the *small-source* case, we replaced the 1.25 cm baseline source tube (constructed from type M copper pipe) with a smaller source tube with inner diameter of 0.32 cm (constructed from 22 gauge stainless steel). In non-dimensional terms, we computed the quantity d_s/M as the ratio of source tube diameter d_s to the turbulence grid mesh size M. This can be thought of as an approximation of the source size relative to the integral length scale, which we estimated as the grid mesh size.

In the *near-bed* case, we inserted a false floor adjacent to the source tube to release the odor adjacent to a boundary. Specifically, we used a section of black foam core, 3/16 inch thickness, as a physical boundary in the wind tunnel. The piece spanned the full 50-cm width of the test section, and extended from 15 cm upstream of the source tube outlet to the end of the test section, a total length of 75 cm. Note that we do not expect the flow in this case to represent a fully developed turbulent boundary layer; the 15 cm development length with the source tube 'obstacle' and upstream turbulence grid complicate the flow beyond a typical flat-plate boundary layer configuration. Rather than a study of dispersion in a developed turbulent boundary layer, our goal in the current work is to obtain data that mimics odor plumes potentially encountered in the real world, which includes complex flows with various proximity to boundaries.

For the *diffusive* release, we fitted the end of the source release tube with a 5-micron diffuser stone (Oxidation Technologies). The cylindrical stone has length 1 inch and diameter 1/2 inch and is constructed from sintered stainless steel. Emitting the odor using a diffusing stone minimizes the release momentum, as in the case of, for example, a flower passively releasing odor into the air.

To create a *buoyant* plume, we increased the fraction of helium in the carrier gas used for the acetone vaporization. Details regarding mixture percentage computations are provided in Appendix D. We used three mass flow controllers to precisely control

the mixture fractions in the plume: one for the flow of helium into the vaporization tube, one for the flow of air into the vaporization tube, and one to control the (typically small) flow of air through the PIV seeding reservoir to mix DEHS aerosols into the plume. We used the densimetric Froude number $\mathrm{Fr_d}$ for non-dimensional parameterization of the plume buoyancy. Fr_d is the ratio of inertial to buoyant effects: $\overline{u}/\sqrt{g'L}$, where g' is the reduced gravity $g(\rho_0 - \rho_s)/\rho_0$, where ρ_0 is the density of the background air and ρ_s is the density of the source, and L is a characteristic length. For this case L is chosen to be the odor source tube diameter, such that $\mathrm{Fr_d} = 1$ represents a neutrally buoyant plume.

In the *fractal grid* case, we installed a fractal turbulence grid to replace the baseline regular square grid (still positioned 15 cm upstream of the source release). The regular square grid had mesh size of 25 mm and bar thickness of 4 mm, while the fractal grid had an effective mesh size of 30 mm with minimum bar thickness 6 mm and maximum bar thickness 17.5 mm. Additional turbulence grid details are provided in Appendix E. For non-dimensional parameterization, we computed the mesh Reynolds number for each grid as $\mathrm{Re_M} = \overline{u}M/\nu$.

case ID	$\mathbf{d_s/M}$	**boundary**	**release velocity**	$\mathrm{Fr_d}$	**grid**	$\mathrm{Re_M}$
Baseline	0.5	freestream	isokinetic	1	square	510
Small-source	**0.2**	freestream	isokinetic	1	square	510
Near-bed	0.5	**near-bed**	isokinetic	1	square	510
Diffusive	0.5	freestream	**diffusive (near-zero)**	1	square	510
Buoyant	0.5	freestream	isokinetic	**4**	square	510
Fractal grid	0.4	freestream	isokinetic	1	**fractal**	**600**

Table 1 Plume conditions for each of the six tested cases, which are identified throughout the manuscript by their case ID listed in column 1. The baseline case is listed on row 1, and each of the other cases changes one parameter from the baseline, emphasized in bold for each row.

3 Results and Discussion

We begin with a statistical characterization of the flow and concentration fields for each case. First, we present the mean and variance of the fields for understanding general plume structure. We then show the single-point probability density functions (PDFs) of concentration at select locations, comparing the distribution with predicted PDF forms identified in the literature. Specific to the concentration field, we also compute intermittency factor, a property known to play a significant role in olfaction contexts (Liao and Cowen 2002; Gumaste et al. 2024). For the velocity field, the turbulence intensity provides insight into the evolution of the decaying grid turbulence and source tube interaction effects across the recorded domain (Mazellier and Vassilicos 2010; Duong and Tavoularis 2024). Combining information from the velocity and concentration fields, we compute the turbulent fluxes to investigate scalar transport mechanisms in the chaotic flow (Warhaft 2000; Rogers et al. 1989; Gotoh and Yeung 2012). Finally, we leverage the time-resolved datasets to compute finite-time

Lyapunov exponent (FTLE) fields, providing a means of clearly visualizing the connection between the Lagrangian structures in the flow field and the evolution of the odor filaments.

3.1 Characterization of the velocity and concentration fields

Representative distributions of the instantaneous velocity and concentration fields are shown in Fig. 3. The variation in these instantaneous snapshots demonstrates the sensitivity of the plume dispersion behavior to the source configuration and flow field properties. All cases exhibit odor concentrations above noise levels across the entire 30 cm domain with filamentous structures that exhibit varying degrees of mixedness and lateral plume dispersion into the ambient air. The noise level statistics for out-of-plume regions for each case are listed in Table 2. For the velocity field, the velocity field vectors show more variation across the domain in the fractal grid case than any of the other configurations.

case ID	**RMS noise**	**variance**
Baseline	0.006	7×10^{-6}
Small-source	0.004	3×10^{-6}
Near-bed	0.008	4×10^{-6}
Diffusive	0.014	8×10^{-6}
Buoyant	0.007	12×10^{-6}
Fractal grid	0.004	4×10^{-6}

Table 2 Root-mean-square (RMS) noise and variance computed in out-of-plume regions for each case, in units of C/C_0.

Phenomenologically, we can draw inferences from the snapshots in terms of the relative importance of two processes in turbulent transport: 1) meandering, in which relatively large eddies move the bulk plume's center of mass, and 2) relative dispersion, in which relatively small eddies spread the plume wider in the lateral direction in a process that can be well-modeled by a diffusive process with an effective diffusivity (also referred to as 'turbulent diffusivity' or 'eddy diffusivity') (Gifford 1959; Cassiani et al. 2020). Smaller source sizes relative to the flow length scales typically extend the meandering regime of the plume. In Fig. 3, we observe primarily meandering behavior in the small source case as well as the fractal grid case, which introduces larger length scales in the flow field relative to the source size. Widening the plume relative to the flow scales, on the other hand, increases the contribution of relative dispersion, as in the diffusive release case. Increasing buoyancy of the plume results in a longer residence time due to the buoyant forces acting opposite to the mean flow, which also induces shear at the plume edges. Both of these effects enhance relative dispersion, resulting in a wider plume with more diffuse filaments of odor. For the near-bed case, the source centerline elevation can be estimated as 6 viscous wall units ($zu_\tau/\nu \approx 6$, where we estimate shear velocity u_τ as 5% of the freestream velocity) from the false floor of the wind tunnel. This approximation assumes a fully developed turbulent boundary layer; here, more complex considerations arise because the leading edge of

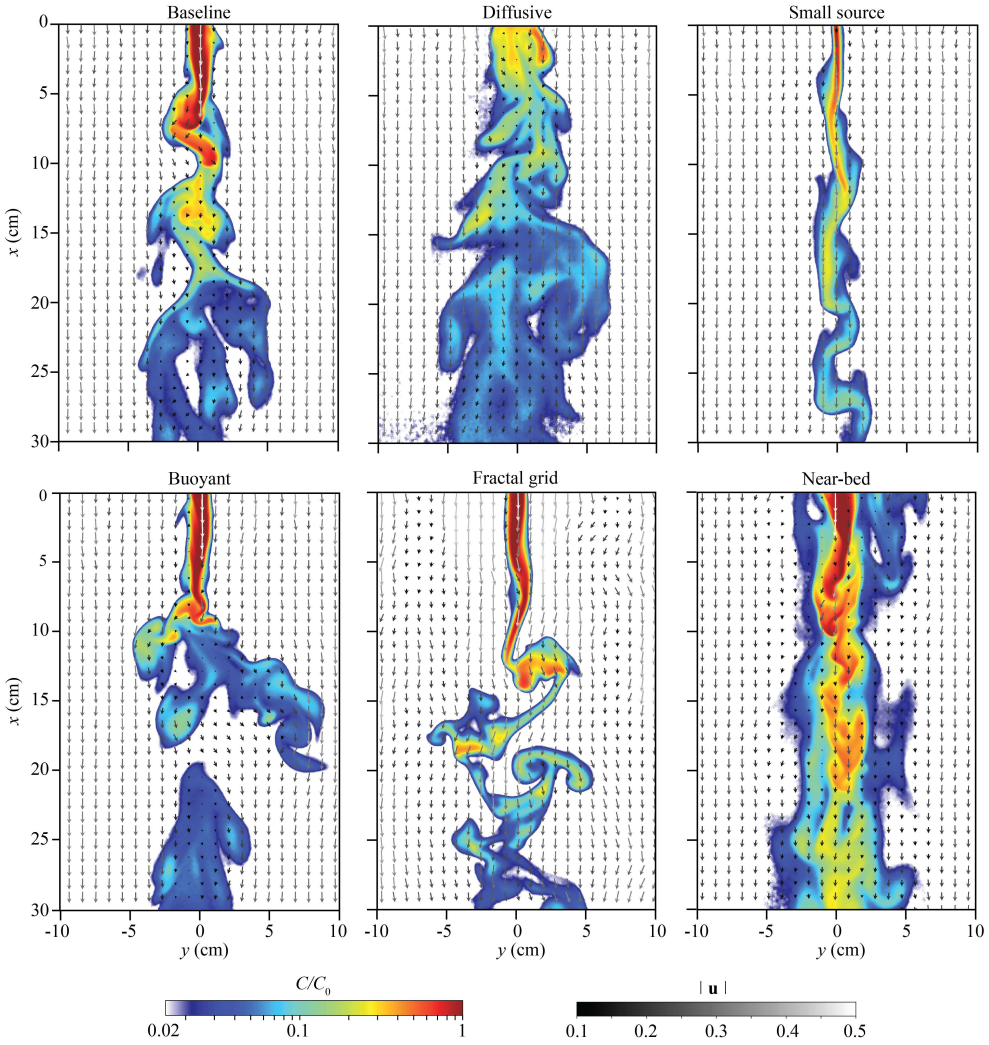


Fig. 3 Instantaneous spatial distributions of velocity (grayscale arrows) and normalized concentration data (color shading) for the six selected cases at a representative instant in time.

the false floor is located a short distance (15 cm) upstream of the top of the FOV, a turbulence grid induces other fluctuations in the flow, and the source itself acts as an obstacle atop the boundary. We do clearly observe that this release location is at least partially outside the viscous sublayer of the turbulent boundary layer (evidenced by the presence of filamentous plume structures rather than smooth transport dominated by viscous mechanisms).

The time-averaged velocity and concentration data for each case are presented in Fig. 4. We first observe that the flow within the plume envelope is affected by the

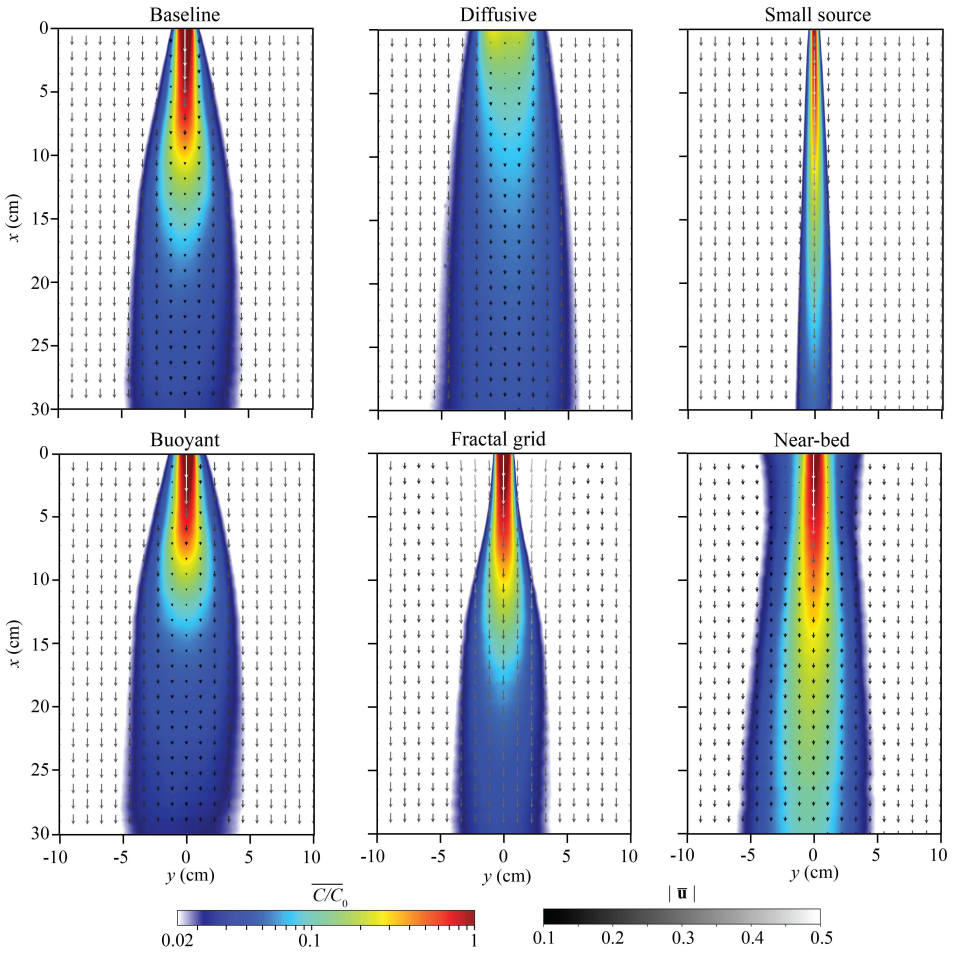


Fig. 4 Time-averaged spatial distributions of velocity (grayscale arrows) and normalized concentration (color shading) for each plume configuration case.

source configuration, more specifically, that in all but the small source and fractal grid cases, the average velocity in the downstream direction is noticeably reduced within the plume envelope. This reduction likely stems from the mean shear along the source tube, which then induces wake structures downstream of the opening. In wake-dominated flows, we expect such reduction in the mean downstream velocity in the wake region. Conversely, in the fractal grid and small source cases, the source size is smaller relative to the integral scales in the flow, which we would expect to reduce the relative importance of the wake structures. The data is consistent with this behavior, further supporting the hypothesis of wake-dominated flows reducing the mean velocities downstream of the source for the baseline, diffusive, and buoyant cases. Note that this interaction between the flow field and source tube represents

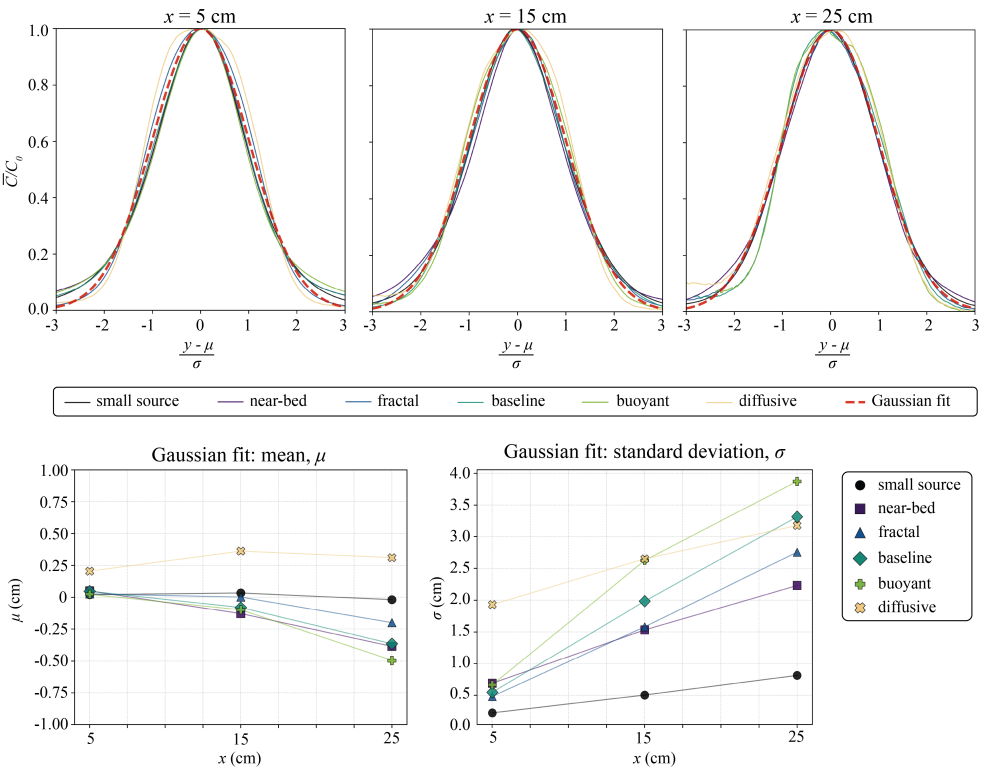


Fig. 5 Lateral profiles of mean normalized concentration at x =5, 15, and 25 cm downstream of the odor source.

an intentional design choice to reflect naturalistic conditions in which odor sources are typically physical objects that will affect the flow field that carries the plume downstream. As illustrated in these datasets, such interaction can play an important role in the statistical properties and dynamics of the velocity and concentration fields, and thus we include these effects as part of the experimental design.

To investigate the cross-stream shape of the mean plumes, lateral profiles of time-averaged concentration at select x-locations are shown in Fig. 5. The profiles were normalized by the local maximum concentration and shifted such that the peaks align at $y = 0$, then the lateral spread was normalized by the standard deviation obtained from a Gaussian fit. The fitting parameters, μ and σ, for each plume configuration are included in Fig. 5. All cases and locations demonstrate distributions consistent with a Gaussian mean plume, with the exception of a slightly wider peak in the near-field ($x = 5$ cm) of the diffusive case. The flatter peak of the profile in this case is to be expected, since the diffusing stone releases odor outward in both the stream-wise and cross-stream directions from the source, inducing an initially wider distribution that persists close to the source. For all other distributions, the self-similar shapes and lack of skewness across the profile demonstrate that the PLIF data does not exhibit any

systematic bias from light sheet variation or laser absorption. The parameterization of the Gaussian fits reveals additional plume characteristics (lower plots in Fig. 5). The mean location of the plume shows a small (< 1 cm) drift in the negative y-direction for most cases (the small source case remains centered on zero and the diffusive case appears to emit a plume biased in the positive y-direction at the source, likely due to inhomogeneities in the diffusing stone). This lateral drift of the bulk plume indicates a small net cross-stream bias in the velocity field, which can be explained by the geometry of the recirculating wind tunnel inducing large-scale structure in the flow field that persists through the flow straighteners and into the test section.

While the mean plume shows overarching trends in the velocity and concentration fields, the fluctuations in the fields drive the intricate structures that mix the plume with the surrounding air. For the velocity field, we visualize fluctuations using the turbulence intensity, defined as the root mean square (RMS) of the fluctuating velocity field normalized by the mean velocity (Fig. 6). We observe two distinct features in the intensity fields. First, we identify a faint signature of the grid turbulence, which induces highest turbulence intensity at the top of the domain that decays with downstream distance. This feature is much stronger in the fractal case, which shows notably higher turbulence intensity generated by the grid. This is expected, since a design feature of fractal grids is the generation of higher turbulence intensities for the same flow speed and downstream location compared to regular grids with similar shape parameters (such as effective mesh size and blockage ratio). The second feature involves turbulent fluctuations driven by the shear layer of the source itself, which causes a boundary layer to develop along the source tube and generates a wake structure that propagates downstream. In all but the fractal case, these structures forming off the source tube show much higher intensity than the surrounding grid turbulence. Importantly, these effects on the flow field due to interaction with a physical source tube represents a design choice that reflects naturalistic conditions, in which odor sources typically emanate from physical sources that influence the development of the flow field. The turbulence intensity plots may also indicate a bifurcation of the evolving flow structures related to the source wake, due to oscillations in the flow emerging from the source tube (future studies can further investigate this effect). For additional details on the turbulence grids and downstream development of length scales, turbulent kinetic energy (TKE), and TKE dissipation rate in the flow, see Appendix E.

To understand the concentration fluctuations, we plot the RMS of the fluctuating concentration (equivalent to the variance of the field) across the domain, shown in Fig. 7. The variance of the concentration field shows a distinct bimodal distribution in the cross-stream direction, most pronounced in the near-field ($x = 5$ cm) and approaching uni-modal in the far-field ($x = 25$ cm). These trends become especially apparent in the lateral profiles of the concentration field variance, shown in Fig. 8. This bimodal pattern is typical of a configuration in which the plume is wide relative to the integral length scales in the flow (Connor et al. 2018; Rahman and Webster 2005; Bara et al. 1992). Intuitively, the pattern results from a 'core' section of the plume that stays at a relatively stable concentration, with peaks on either side of this core zone. The small-source case, on the other hand, shows an approximately unimodal distribution even in the near field ($x = 10$ cm), since the plume is not wide enough to have an area

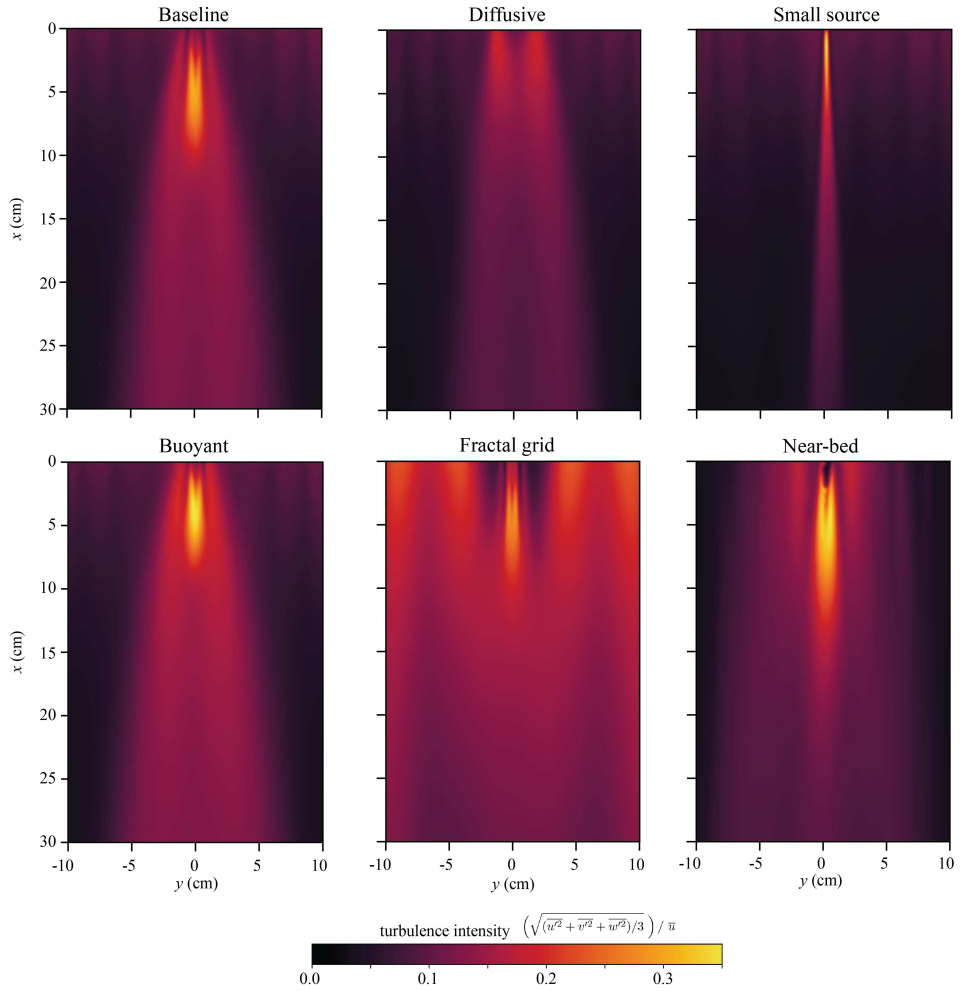


Fig. 6 Spatial distributions of turbulence intensity for each plume configuration case.

of relatively consistent concentration as it meanders. We also see in the cross-stream profiles that the diffusive case shows the lowest variance, since the diffusive source emits a wide plume with shallower gradients that yields lower variance with the same amount of movement.

The scalar variance discussed above results in a highly intermittent plume, that is, a plume in which the concentration field exhibits long periods of very low concentration at a given location. This long-tailed nature of the concentration distribution is a key characteristic in the context of olfactory navigation, as animals have been shown to detect and respond to intermittency while searching for an odor source (Gumaste et al. 2024). We quantify it using the intermittency factor (Wilson et al. 1985), defined as the empirical probability, $\mathbb{P}$, that the concentration is above a given threshold C_T,

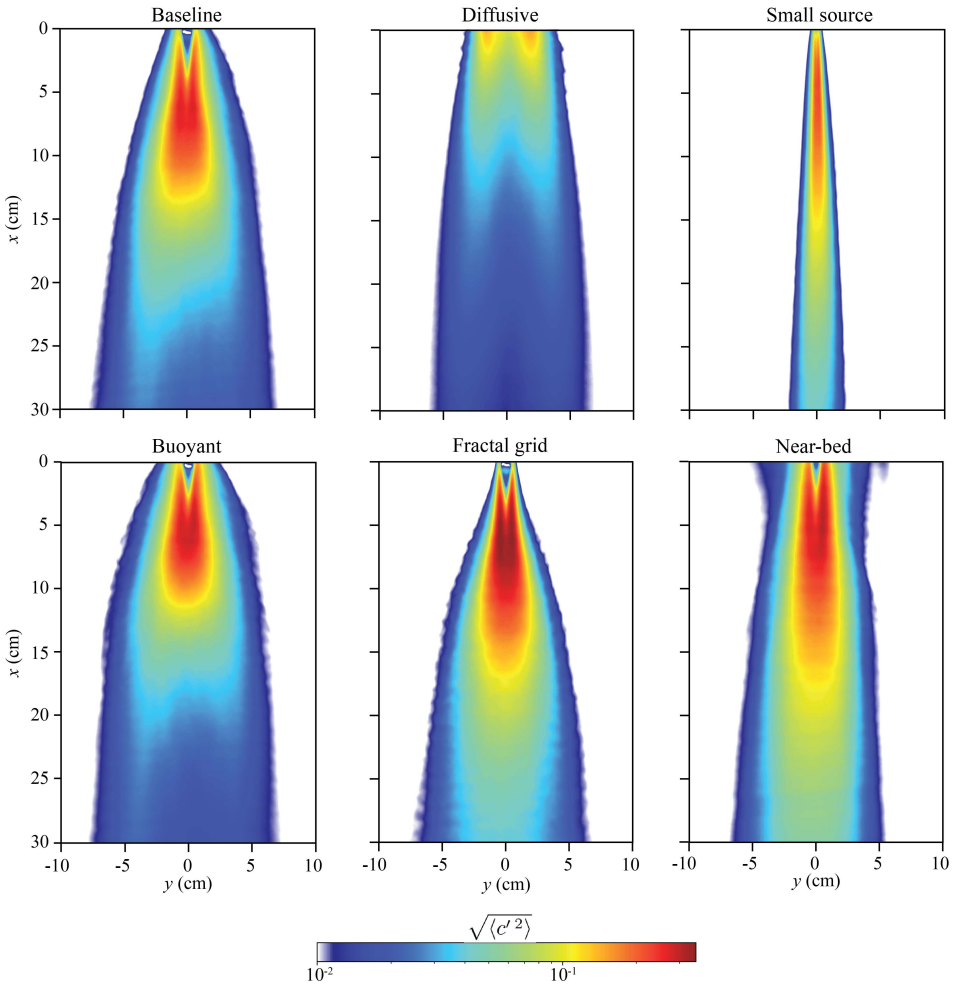


Fig. 7 Spatial distributions of root-mean-square (RMS) normalized concentration fluctuations for each plume configuration case.

equivalent to the fraction of time that the concentration exceeds the threshold:

$$\gamma \equiv \mathbb{P}(C > C_T) = \frac{1}{N} \sum_{n=1}^{N} \mathbb{I}[C_n > C_T] \tag{4}$$

where N is the total number of frames in the time series, C_n is the concentration on the n^{th} time step, and $\mathbb{I}$ is the indicator function, equal to 1 if true and 0 if false. Here we choose C_T to be 0.02 to ensure that the plume is well-differentiated from the background level of acetone vapor. The resulting intermittency contours are shown in Fig. 9. Plumes that are relatively well-mixed across a wide area at the

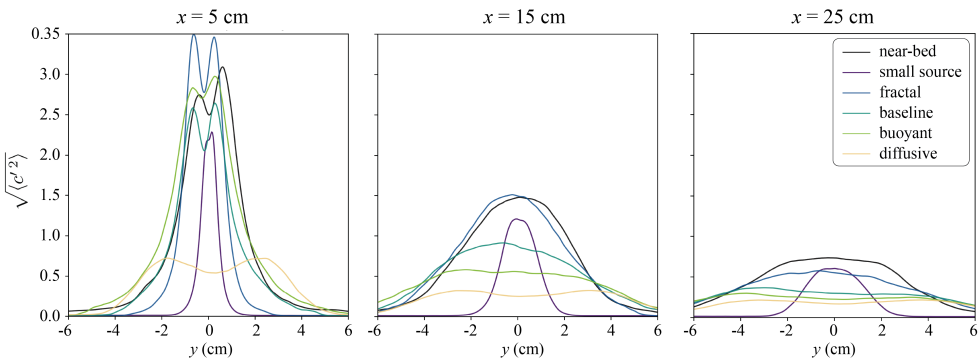


Fig. 8 Lateral profiles of RMS normalized concentration fluctuations for each plume configuration case at x =5, 15, and 25 cm downstream of the odor source.

source, e.g., the diffusive and near-bed cases, show little streamwise variation in the intermittency factor. On the other hand, plumes that experience a wide meandering path relative to the plume width, e.g., the fractal case, show a significantly declining intermittency factor streamwise along the plume center, indicating a 'patchier' plume as distance from the source increases. In all cases, the intermittency factor increases from lateral locations toward the centerline of the plume, indicating a common trend in the spatial distribution of intermittency factor relative to the source location. Such spatial encoding of source location information provides a potentially useful cue for olfactory navigation strategies that leverage intermittency.

Next, we expand consideration of the concentration beyond binary categorization to investigate the entire probability distribution functions (PDFs) of concentration values. The single-point PDFs for select cases at two downstream locations along the centerline are shown in Fig. 10, and at two downstream locations offset 2 cm from the centerline are shown in Fig. 11. In general, the PDFs exhibit long-tailed right-skewed distributions, as is common in turbulent mixing, with peaks located at low concentration values. Along the centerline, locations closer to the source (top row of Fig. 10) show a wider range of concentration values (note the differing x-axis between the top and bottom rows) with a much higher likelihood of encountering larger concentrations of odor compared to downstream location. Intuitively, as the plume moves downstream, molecular diffusion and turbulent dispersion work to decrease concentration values and increase the likelihood of periods with zero concentration. For the locations off-center of the plume (Fig. 11), the PDFs in the upstream position (top) show that the high-concentration areas of the plume rarely meander 2 cm away from the plume centerline, since the PDFs no longer span into higher values. The PDFs in the downstream position (bottom), however, are very similar to those along the centerline at the same downstream location. This similarity indicates that by $x = 30$ cm, the plume has dispersed widely enough that the concentration field shows similar statistics within a central region that spans at least +/- 2 cm from the centerline.

To further characterize the concentration PDFs, we follow the approach of several studies that point toward universality of the Gamma distribution for scalar PDFs in

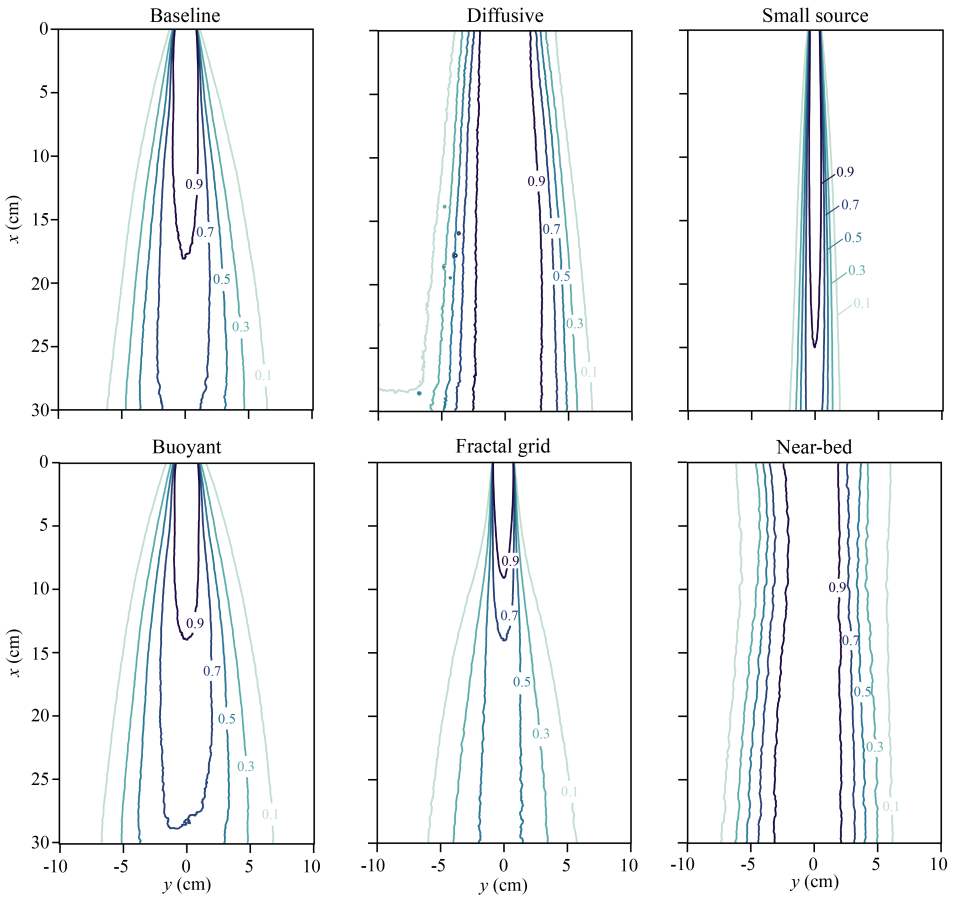


Fig. 9 Intermittency contours for normalized concentration for each plume configuration case.

turbulent boundary layers (Nironi et al. 2015; Duplat and Villermaux 2008; Yee and Skvortsov 2011). Specifically, it has been found that the following Gamma distribution function aligns well with data under varied conditions, when parameterized by $k = i_c^{-2}$, where i_c is the local fluctuation intensity value, computed as $i_c = \sigma_c/\overline{c}$ (where σ_c is the standard deviation of concentration fluctuations):

$$p(\chi) = \frac{k^k}{\Gamma(\chi)} \chi^{k-1} \exp\left(-k\,\chi\right) \tag{5}$$

where $\Gamma(\cdot)$ is the Gamma function, and $\chi \equiv c/\overline{c}$.

As evidenced in Figs. 10 and 11, the computed Gamma distribution provides a good description of the PDF behavior across cases and locations. To be clear, the overlaid Gamma distribution is not a fitted curve, but rather a computed Gamma distribution solely parameterized by fluctuation intensity. As shown by Nironi et al. (2015), the fluctuation intensity is directly linked to the intermittency factor, providing intuition

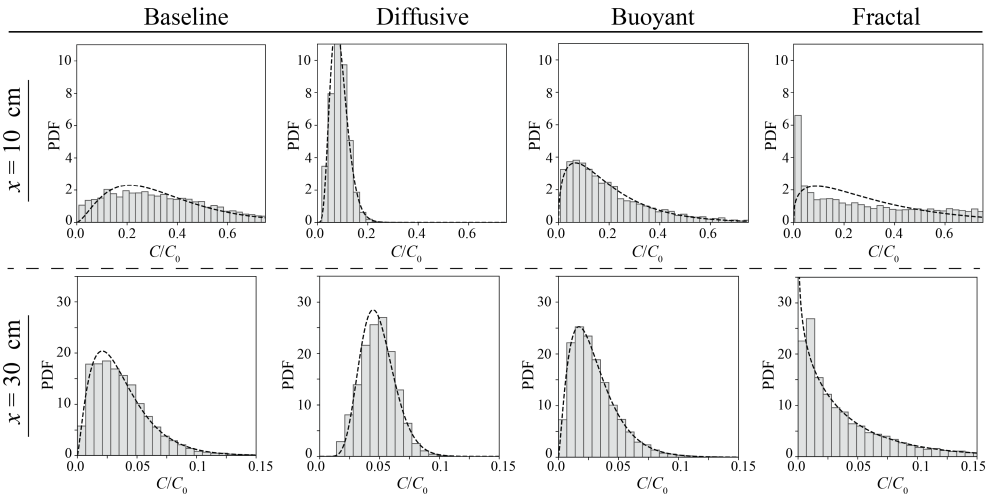


Fig. 10 Probability density function of normalized concentration along the centerline of the plume ($y = 0$) at x =10 and 30 cm downstream of the odor source, for four plume configuration cases. Overlay of Gamma distribution parameterized by the local concentration intermittency.

on the importance of intermittency as a parameter in olfactory navigation contexts. More generally, the spatial variation in PDF shape across plume locations implies spatial encoding of source information within the concentration PDF.

3.2 Quantities relating the flow and odor data

The synchronized nature of the experiments allows us to directly compute quantities that relate the velocity and concentration fields at a given instant in time. Turbulent fluxes may provide particularly relevant insight for olfactory navigation as these quantities relate to the direction of the motion of odor, a quantity found to be detected and utilized by searching animals (though as statistical quantities, the turbulent fluxes themselves may or may not be directly relevant during olfactory navigation) (Kadakia et al. 2022). The turbulent fluxes are defined as the time-averaged product of concentration and velocity fluctuations in each direction: $\overline{c'u'}$, $\overline{c'v'}$, and $\overline{c'w'}$. As illustrated in Fig. 12, the turbulent fluxes are generally laterally outward from the plume centerline, as is expected in a spreading scalar plume, with higher magnitude near the source and lower magnitudes with increasing downstream distance.

Additionally, the time-resolved nature of the coupled fields allows for computation of Lagrangian quantities via numerical advection of tracer particles. As an example, we compute here the finite-time Lyapunov exponent (FTLE) field to identify areas of the flow that we expect to attract local trajectories, that is, structures in the flow along which we expect odor filaments to form and evolve. Ridges in backward-time FTLE fields indicate the presence of such attracting structures in the flow (Peacock and Haller 2013). To compute the FTLE field, we first advect uniformly seeded particles backward in time using the measured velocity data to determine the flow map ϕ (Shadden et al.

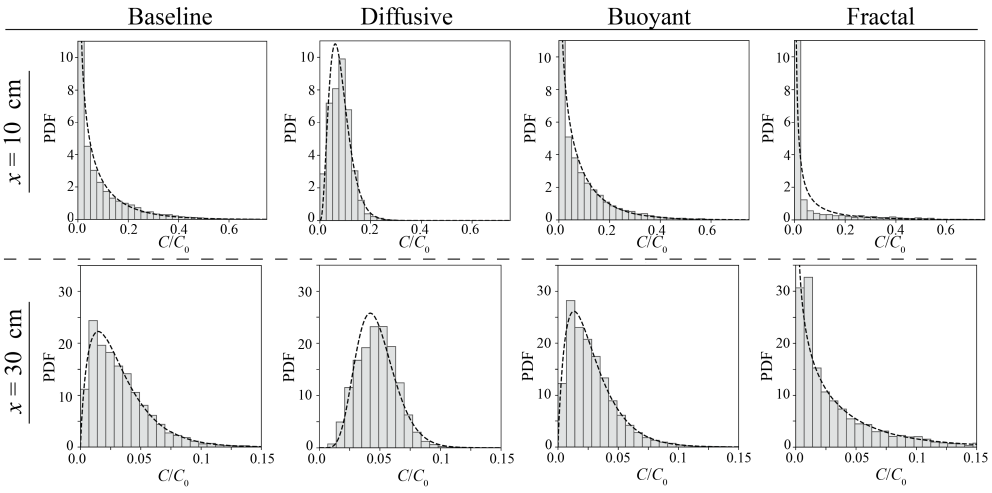


Fig. 11 Probability density function of normalized concentration offset from the plume centerline at $y = 2$ cm, at x =10 and 30 cm downstream of the odor source, for four plume configuration cases. Overlay of Gamma distribution parameterized by the local concentration intermittency.

2005). For our discrete data, the flow map is a set of particle locations with initial positions $\mathbf{x}_{i,j}(t)$ and final positions $\mathbf{x}_{i,j}(t+T)$, where $\mathbf{x}$ is the (x, y) location. We therefore calculate the gradient, $\nabla\phi$, using finite differencing:

$$\left.\frac{d\phi_t^{t+T}(\mathbf{x})}{d\mathbf{x}}\right|_{\mathbf{x}_{i,j}} = \begin{bmatrix} \frac{x_{i+1,j}(t+T)-x_{i-1,j}(t+T)}{x_{i+1,j}(t)-x_{i-1,j}(t)} & \frac{x_{i,j+1}(t+T)-x_{i,j-1}(t+T)}{y_{i,j+1}(t)-y_{i,j-1}(t)} \\ \frac{y_{i+1,j}(t+T)-y_{i-1,j}(t+T)}{x_{i+1,j}(t)-x_{i-1,j}(t)} & \frac{y_{i,j+1}(t+T)-y_{i,j-1}(t+T)}{y_{i,j+1}(t)-y_{i,j-1}(t)} \end{bmatrix}. \tag{6}$$

Next, the right Cauchy-Green deformation tensor, Δ, provides a rotation-independent description of the square of local change in distances due to deformation. We compute it by multiplying the deformation gradient tensor by its transpose as follows:

$$\Delta = \left(\frac{d\phi_t^{t+T}(\mathbf{x})}{d\mathbf{x}}\right)^{\top} \frac{d\phi_t^{t+T}(\mathbf{x})}{d\mathbf{x}} \tag{7}$$

We then determine the maximum eigenvalue of the right Cauchy-Green Deformation tensor, $\lambda_{max}(\Delta)$. The maximum eigenvalue is used in the below equation to compute the FTLE field, $\sigma_t^T(\mathbf{x})$, for integration time T at time t at each position in the particle grid:

$$\sigma_t^T(\mathbf{x}) = \frac{1}{|T|} \ln \sqrt{\lambda_{max}(\Delta)}. \tag{8}$$

We provide an example instantaneous snapshot of the FTLE field overlaid with the concentration field in Fig. 13, illustrating the tendency of the odor filaments to be drawn along the ridges in the FTLE field. Note that because we collected data in a single plane, we computed the 2D FTLE field despite the three-dimensional nature of the

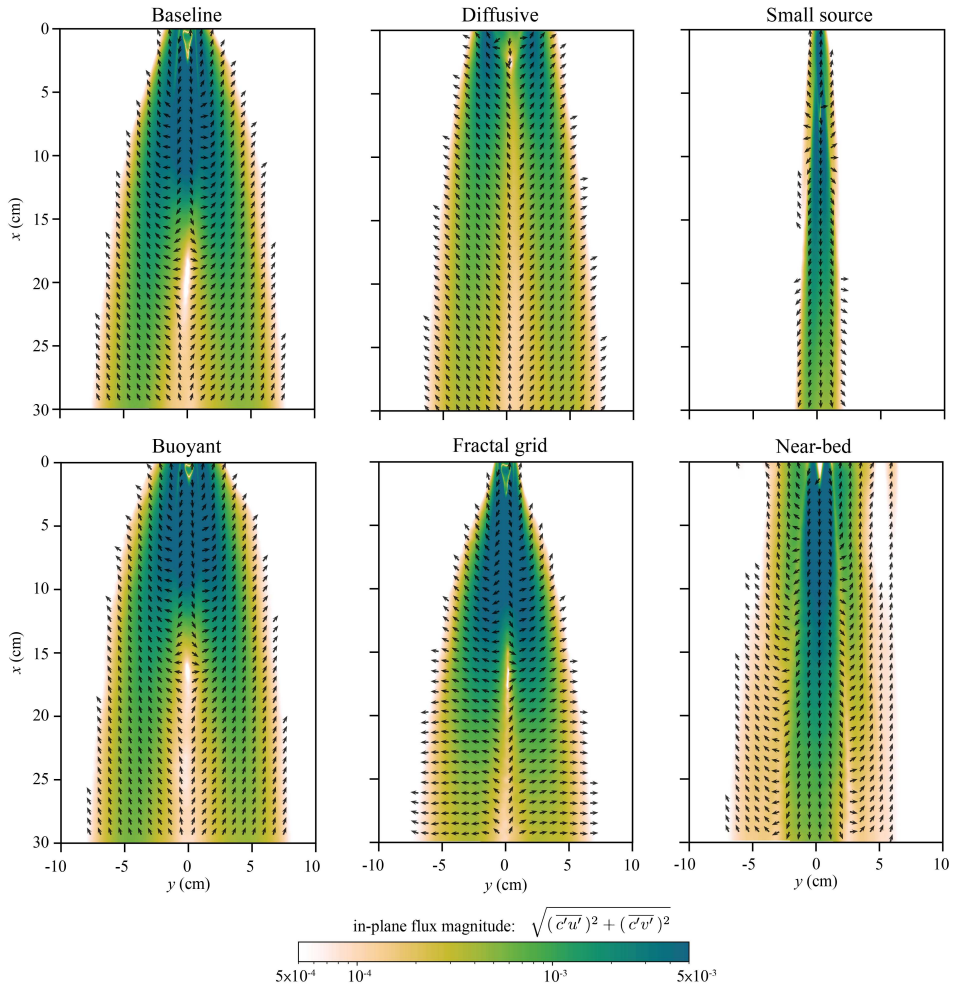


Fig. 12 Spatial distribution of in-plane turbulent fluxes for each plume configuration case. Arrows represent the $[\overline{u'c'}, \overline{v'c'}]$ vector direction, and the color shading represents the magnitude.

plume and flow field. We expect the alignment of the FTLE ridges with the concentration field to be affected to varying degrees across different configurations, depending on the strength of out-of-plane flow field structures. Previous studies have shown that 2D FTLE ridges can show good agreement with those computed using 3D flow field data across many conditions, contingent on small enough values for the vertical shear magnitude and vertical velocity gradient(Sulman et al. 2013; Knutson et al. 2015). Future studies can evaluate these quantities to better understand the fidelity of the 2D FTLE ridges to the true 3D ridges in our specific conditions. Qualitatively, the 2D FTLE ridges we compute show good alignment with the odor filaments, with strongest

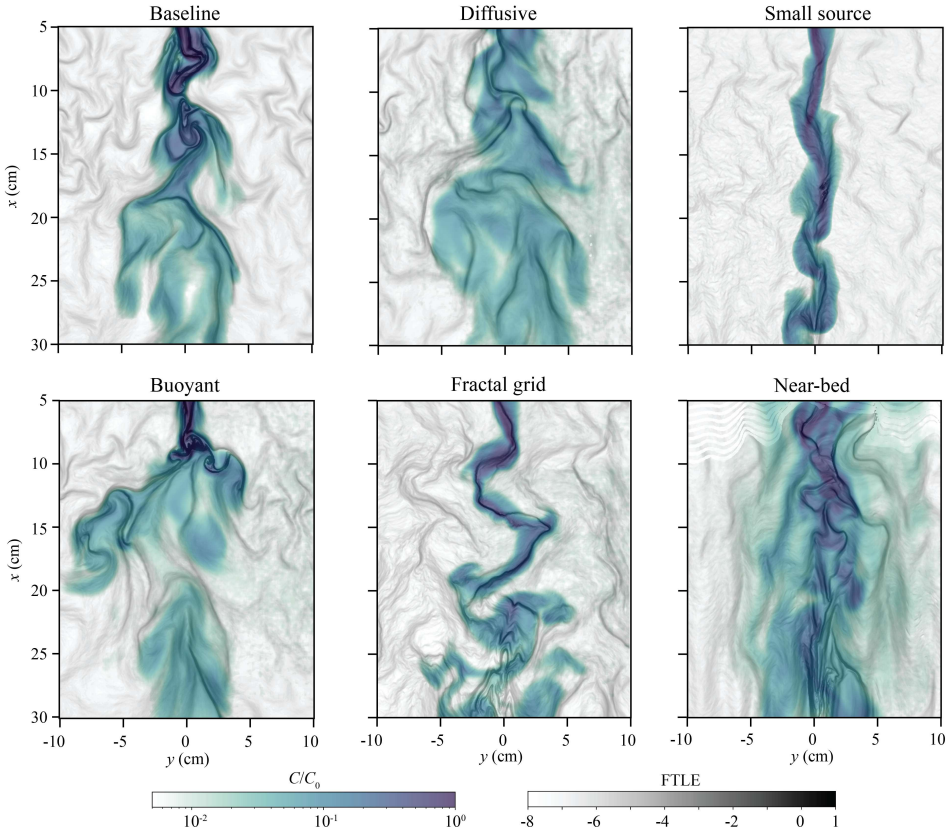


Fig. 13 Finite-time Lyapunov Exponent (FTLE) field overlaid with normalized concentration at a representative instant in time.

alignment for those configurations dominated by chaotic advection away from boundaries (specifically, the fractal, small source, and baseline cases), rather than diffusive processes (the diffusive and buoyant cases) or those with strong mean shear in the out-of-plane direction (the near-bed case). Intuitively, this result stems from the nature of backward-time FTLE ridges as advective boundaries, meaning diffusion allows odor to cross the ridges, despite the asymptotic nature of the attracting boundaries. Future work will investigate the *quantitative* relationships between the FTLE fields and the odor plume structures.

4 Summary

The current study employs a custom-built sPIV and PLIF experimental setup to measure velocity and concentration fields for a passive scalar emitted into chaotic flow field in a low-speed wind tunnel under a variety of conditions. Six datasets are presented in the current work: 1) a baseline case with isokinetic release into a flow field

generated by a regular turbulence grid, along with cases that use 2) a diffusive source, 3) a small source, 4) a buoyant plume, 5) a fractal turbulence grid, and 6) a false floor to create a 'near-bed' condition. The data is recorded at 20 Hz, fast enough to resolve the frame-by-frame evolution of structures in the flow and odor fields. Spatially, sub-millimeter resolution in both fields allows us to measure scales down to the dissipation scales.

Along with demonstrating the instantaneous data characteristics, we compute statistical characterizations (mean, variance, and PDFs) of the plume as well as key properties relevant to olfactory navigation (intermittency, turbulence intensity, turbulent fluxes, and FTLE fields). While some similarities appear across all cases, such as the Gaussian nature of the mean plume and the decay of kinetic energy across the domain, others demonstrate sensitivity to the source configuration and flow field, such as the intermittency distribution and the turbulent flux behavior. Generally, the computed quantities show spatial variation across the domain, indicating some encoding of spatial information within the given signal. We also observe that configurations with length scales in the flow that are large relative to the plume width, i.e. the fractal grid case, show closest adherence to the FTLE structures in the flow field. Finally, the turbulent fluxes show a direction generally pointing outward from the plume centerline, a potentially useful property in navigation for finding the plume centerline.

The methods and measurements from this work may be useful for a broad range of research areas. Considering olfactory navigation applications, these datasets can provide a critical resource in the research of multimodal search strategies (i.e., strategies using information from both the velocity and concentration fields), such as to develop laboratory protocols for naturalistic stimuli in live animal experiments, or as testbeds for artificial navigation algorithms across a range of conditions. Thinking toward fluid dynamics applications, the datasets can help fill a gap in experimental measurements for investigations of turbulent mixing in low-Reynolds number, low-Schmidt number regimes. Real-world measurements of dissipation-scale flow and scalar dynamics in such regimes remains limited, despite the importance of such data in investigating fundamental concepts such as the universality of statistical turbulence properties across Reynolds numbers (Schumacher et al. 2014). The datasets we presented herein may enable progress in these or other fields by providing a time-resolved, high-resolution suite of simultaneous velocity and concentration measurements in an otherwise data-scarce regime.

Appendix A Wind tunnel calibration

The wind tunnel was originally calibrated by the manufacturer using laser Doppler anemometry (LDA), ensuring quality and repeatability of the fan settings to specific wind speeds. However, conditions during actual dataset acquisition are significantly different than those at the manufacturing facility, necessitating different settings to achieve the same wind speeds.

To determine fan settings for the desired wind speeds for our experiments, a wind tunnel calibration was performed in July 2025, using PIV to measure the average velocity at each fan setting. Downstream of the fan, a differential pressure sensor

measures the pressure drop across an orifice plate to quantify the wind speed, reporting the pressure drop in terms of a DC voltage ranging from 0 to 5 V. We varied the fan setting by incrementing the DC voltage measured across the orifice plate in 0.1 V increments. Throughout the calibration, conditions mimicked typical acquisition setup, with a 50 mm diameter orifice plate installed, the activated charcoal filter in place, and a 1-inch square turbulence grid located 15 cm upstream of the source tube outlet. The bulk wind tunnel flow was seeded with DEHS particles, and air seeded with DEHS particles was also released from the source tube isokinetically. We estimated isokinetic release conditions based on previous wind tunnel testing carried out in August 2023. The data was collected at a rate of 10 Hz for two minutes, yielding 1200 frames.

The final calibration curve was also compared to the previous wind tunnel testing to verify repeatability of the settings with these independent tests (Fig. A1). Note that the calibration in 2023 was performed in a horizontal configuration with a honeycomb flow straightener upstream of the source tube, so some variation is expected. The consistency of the results over the course of two years and significant configuration changes provides confidence in the settings used for dataset collection across the configurations in the current study.

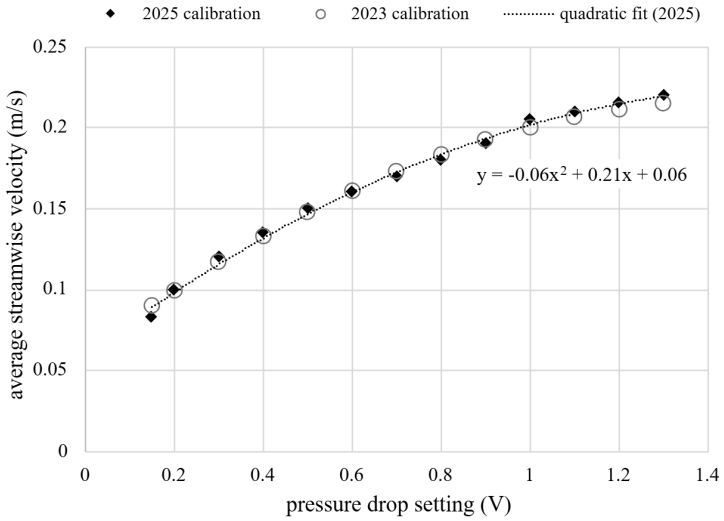


Fig. A1 Plot of wind tunnel calibration in July 2025 (filled diamonds) and August 2023 (open circles), with quadratic fit (dotted line).

Appendix B Source Constancy

A key assumption in the instantaneous source normalization step of the PLIF processing pipeline is that the source remains a constant concentration throughout the experiment. To maintain such a condition, we saturate the carrier gas through vaporization in a long (1.5 m) copper tube. The saturation concentration of acetone vapor

is particularly sensitive to temperature, necessitating a constant temperature at the plume outlet. During the vaporization process, however, the evaporation of liquid acetone to vapor requires heat energy, thus dropping the plume temperature as the acetone vaporizes. To mitigate this, we selected copper material for its high thermal conductivity, and designed the length of the tube to both ensure high vaporization efficiency (expected to be 95% to 99%) and allow for stabilization of the plume temperature to the ambient temperature (via heat transfer from the surrounding environment through the copper walls of the tube).

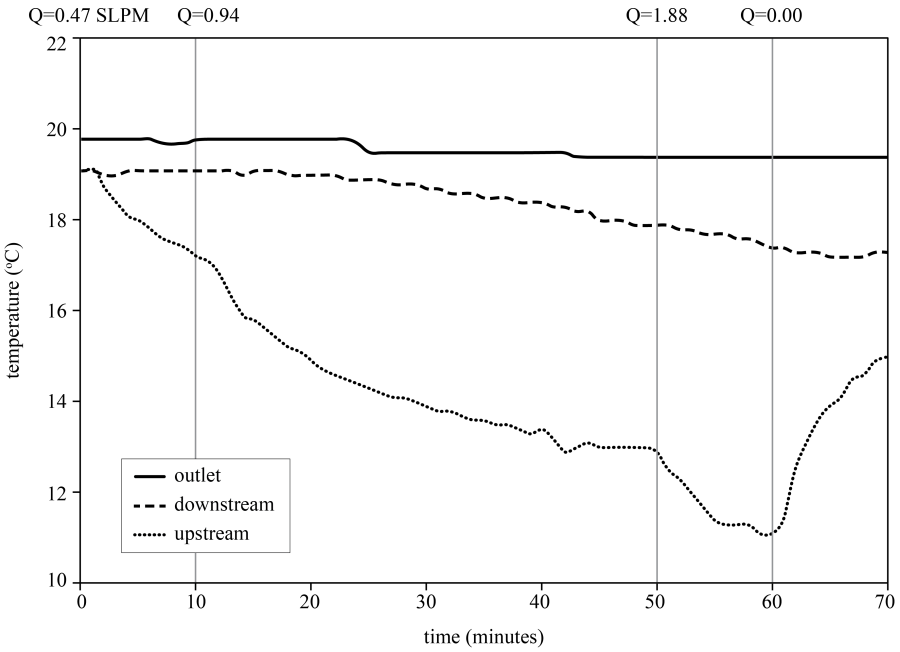


Fig. B2 Temperature recordings of acetone vapor generation tube at three locations: at the upstream end of the tube (solid line), a downstream location (dashed line), and the outlet of the tube (dotted line). Changes to the flow rate, Q, in standard liters per minute (SLPM) are marked with gray vertical lines.

To investigate the thermal stability of our acetone plume generation system, temperature testing was performed using thermistors fixed at three positions along the copper tube: one at the upstream end, one at a downstream location, and one at the tube outlet. The flow rate of carrier gas through the tube was periodically varied throughout the 70-minute test. The results, shown in Fig. B2, demonstrate that despite significant temperature drops at the upstream end of the tube as the acetone vaporizes (8° C over the course of the experiment), the outlet remains an essentially constant temperature (dropping only 0.3° C over the entire test). These results provide confidence that no significant source concentration changes are likely to occur during the 5-minute data acquisition period for our datasets.

Appendix C Energy measurements: PLIF laser heads

The laser heads used for PLIF measurements exhibited energy levels sensitive to changes in daily conditions. Achieving specification-level energy required daily adjustments to the temperature setpoints in the harmonic generator crystals to raise the overall energy as well as decrease the energy difference between the two laser heads in the unit.

Upon startup of the lasers each day of data collection, we first allow a warm-up period of approximately 30 minutes. Next, we tuned the temperature setpoints for the second harmonic (2ω) and 4th harmonic (4ω) generator crystals using an iterative process. During the tuning process, we continually measured the energy output of the lasers using an Ophir® pyroelectric energy sensor (model PE25BF-DIF-C) with StarLab 3.80 software. We began at a setpoint about 0.5°C lower than the expected optimal temperature, then slowly raised the temperature, observing the changes to energy levels. Typically, we observed that changes to the 2ω crystal affected the difference between energy output of the two laser heads, while changes to the 4ω crystal affected the overall magnitude of the energy. However, the two setpoints affected each of these quantities in sometimes unpredictable ways. Between each change of temperature setpoint, we waited at least five minutes for the energy level to stabilize prior to a new adjustment. When satisfactory energy levels were achieved, we monitored the energy levels for at least 20 minutes to ensure energy levels remained consistent. Using this iterative process, we were able to achieve steady energy output of approximately 100 mJ or higher during the dataset collection. Figure C3 shows two minutes of the energy data following setpoint tuning for each of the days during which final datasets were collected. Table C1 shows the mean and standard deviation for each of the time series. These values demonstrate the steady, high energy levels achieved using this technique.

Date	Mean (mJ)	Standard Deviation (mJ)
8-29-2025	98.6	6.9
9-10-2025, pre-sample	113.5	3.2
9-10-2025, post-sample	107.7	3.9
9-26-2025, pre-sample	111.1	4.1
9-26-2025, post-sample	105.7	3.6
10-01-2025	107.6	3.7

Table C1 Mean and standard deviation of 2-minute samples from QSmart Twins laser heads.

We also performed one set of adjustments to the beam alignment between the two laser heads, approximately two weeks prior to final dataset collection. Following procedures specified in the QSmart Twins manual, we tuned the alignment to ensure satisfactory overlap in both the near field and far field of the laser beams.

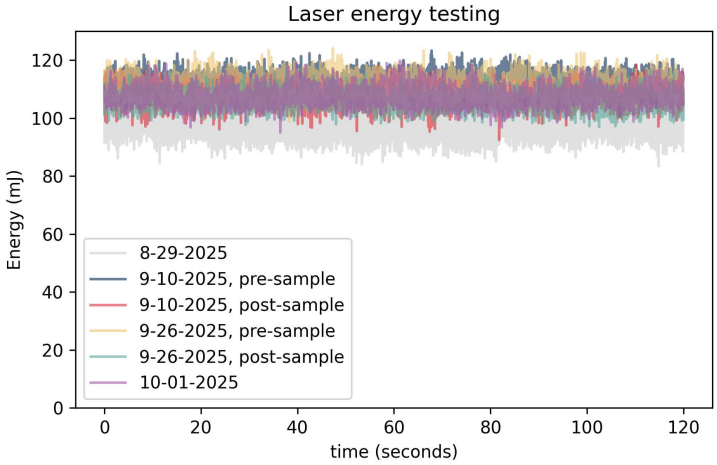


Fig. C3 Qsmart Twins dual-laser energy readings for two minute samples on each day of final dataset collection. On days with two samples, one sample was taken prior to data collection and denoted as "pre-sample", while the other was taken after data collection and denoted as "post-sample."

Appendix D Buoyancy computations

We can frame the goal of changing plume buoyancy in terms of controlling the specific gravity (SG) of the gas mixture, defined as

$$\mathrm{SG} = \frac{\rho_{\mathrm{ace}} x_{\mathrm{ace}} + \rho_{\mathrm{He}} x_{\mathrm{He}} + \rho_{\mathrm{CDA}} x_{\mathrm{CDA}}}{\rho_{\mathrm{air}}}, \tag{D1}$$

where x is the volume fraction of each component gas in the mixture and ρ is its density, with subscripts 'ace' for acetone, 'He' for Helium, 'CDA' for compressed dry air, and 'air' for the ambient laboratory air. We distinguish between CDA and air because the air for the acetone carrier gas comes from a facilities compressed gas line, which has negligible humidity, while the ambient air into which the plume is injected has some humidity, which changes the air density. To compute the ambient air density, we can use:

$$\rho_{\mathrm{air}} = \frac{P_{\mathrm{dry}} M_{\mathrm{dry}} + P_{\mathrm{H_2O}} M_{\mathrm{H_2O}}}{RT}$$

where P is partial pressure, M is molar mass, R is the universal gas constant (0.0821 L atm mol^{-1} K^{-1}), and T is the temperature, with subscripts 'dry' and 'H_2O representing dry air and water, respectively. For dry air (and CDA), we use a molar mass of 28.96 g/mol (Jones 1978). To compute the partial pressure of water, we multiply the relative humidity by saturation pressure of water, which is found using the Antoine equation, shown in equation 5, using the empirical constants for water (A=5.40221, B=1838.675, and C=241.413, see (Linstrom 1997)).

For determining the mass flow rates, we want to compute the initial number of moles of each species to reach the desired specific gravity. First, we need to know the partial pressure of saturated acetone vapor, which comes from the Antoine equation:

$$\log_{10} P_{\text{sat}} = A - \frac{B}{T + C} \tag{D2}$$

where P_{sat} is the vapor pressure in bar, T is temperature in degrees Celsius and with empirical constants A=4.42, B=1312.25, and C=240.71 for acetone (see (Linstrom 1997))

Assuming we reach 95% of the saturated concentration of acetone due to the long residence time of the copper tube, the volume fraction of acetone can be calculated as $0.95 * P_{\text{sat}}/P_{\text{atm}}$. In Boulder, the ambient pressure P_{atm} is approximately 0.82 atm = 0.83 bar. In table D2, we compute the volume fraction for two temperatures based on the expected range of experimental conditions, likely from around 15 to 20 degrees C (59 to 68 degrees F).

Table D2 Acetone partial pressure and mole (volume) fraction at 95% saturation.

Temperature	Vapor pressure (bar)	volume (molar) fraction
15	0.186	0.225
20	0.234	0.282

Now we need to solve for the fraction of air and helium given the desired specific gravity. Below we show an example computation for neutral buoyancy, that is, a specific gravity of unity:

$$\text{SG} = \frac{\rho_{\text{ace}} x_{\text{ace}} + \rho_{\text{He}} x_{\text{He}} + \rho_{\text{CDA}} x_{\text{CDA}}}{\rho_{\text{air}}}$$
$$\rho_{\text{air}} = \rho_{\text{ace}} x_{\text{ace}} + \rho_{\text{He}} x_{\text{He}} + \rho_{\text{CDA}} x_{\text{CDA}}$$

subject to $x_{\text{ace}} + x_{\text{He}} + x_{\text{air}} = 1$. We then substitute known molar masses in g/mol and the 95% saturated acetone vapor molar fraction for x_{ace}. Solving for x_{CDA}, we have:

$$\begin{aligned}
M_{\text{air}} &= M_{\text{ace}} x_{\text{ace}} + M_{\text{He}} x_{\text{He}} + M_{\text{CDA}} x_{\text{CDA}} \\
M_{\text{CDA}} x_{\text{CDA}} + M_{\text{He}}(1 - x_{\text{CDA}} - x_{\text{ace}}) &= M_{\text{air}} - M_{\text{ace}} x_{\text{ace}} \\
M_{\text{CDA}} x_{\text{CDA}} - M_{\text{He}} x_{\text{CDA}} &= M_{\text{air}} - M_{\text{ace}} x_{\text{ace}} - M_{\text{He}} + M_{\text{He}} x_{\text{ace}} \\
x_{\text{CDA}} &= \frac{M_{\text{air}} - M_{\text{ace}} x_{\text{ace}} - M_{\text{He}} + M_{\text{He}} x_{\text{ace}}}{M_{\text{CDA}} - M_{\text{He}}}, \quad \text{and} \\
x_{\text{He}} &= 1 - x_{\text{CDA}} - x_{\text{ace}}
\end{aligned}$$

Using the the molar fractions, we can then determine the mixture percentages for the current laboratory conditions (temperature and humidity) and gas-specific flow rates to achieve the desired specific gravity.

Appendix E Grid turbulence characteristics

We used two different turbulence grids for inducing turbulent fluctuations in the velocity flow field: a regular grid and a fractal grid. Note that our aim was not to parameter-match the grids for a formal investigation of the plume dispersion effects of different grid geometries, but rather to leverage the two different geometries to generate a diversity of spatiotemporal plume structures. In this Appendix, we present design details of each grid and explore the resulting flow field characteristics.

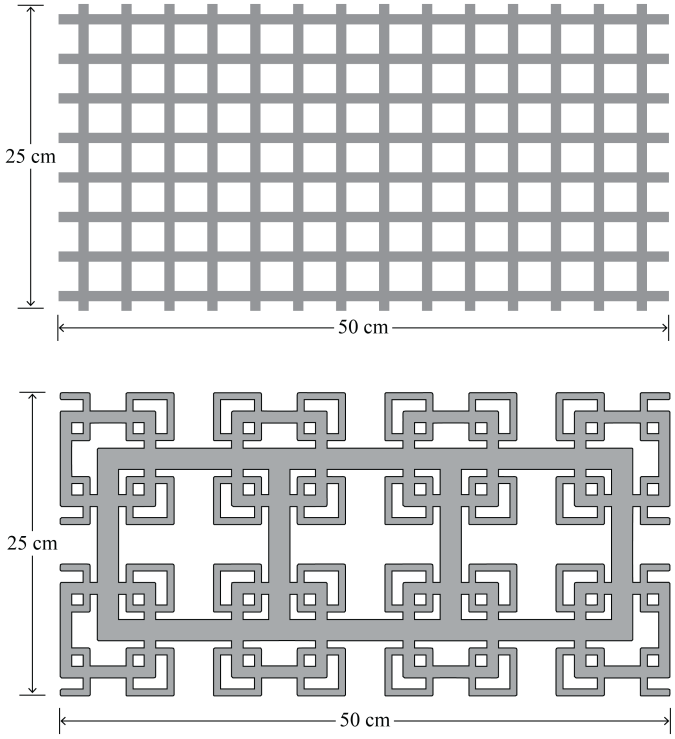


Fig. E4 Scale drawings of the regular turbulence grid (top) and fractal turbulence grid (bottom) used in the experimental configurations.

For the cases that used a regular grid, we installed the passive square turbulence grid shown in the top of Fig. E4, a machined aluminum grid. The grid has a mesh size, M, of 25 mm, and a bar thickness of 4 mm. The blockage ratio of the grid, defined as the ratio of the area of the solid portion of the grid to the total cross-sectional area of the grid, is approximately 0.22.

For the fractal case, we induced turbulent fluctuations in the flow field using a fractal turbulence grid with a square pattern (shown in the bottom of Fig. E4), generating turbulence intensity that decays with downstream distance from the grid. Fractal

grids are parameterized by the number of fractal iterations, N, the bar lengths L_j and thickness t_j at iteration j, and the number of patterns, B, at each iteration. For our grid, $N = 3$ and L_1, L_2, and L_3 are 16, 8, and 4 cm, respectively. Due to the rectangular nature of the wind tunnel cross-section, we identify B based on the central 25 $\times$ 25 cm square of the fractal grid, for which $B = 4$. The properties of the generated flows strongly depend on the grid's fractal dimension, D_f, effective mesh size, M_{eff}, and thickness ratio, t_r (Hurst and Vassilicos 2007). The fractal dimension is defined as $D_f = \log B / \log(1/R_L)$, where R_L is the ratio of bar length from one iteration to the next; in our case, $R_L = 1/2$ and $D_f = 2$ (a space-filling configuration). The effective mesh size is defined as $M_{\text{eff}} = \frac{4T^2}{P}\sqrt{1-\sigma}$, where T^2 is the area of the wind tunnel, P is the fractal perimeter, and the blockage ratio σ is the ratio of area blocked by the grid bars to the total cross-sectional area of the grid. For the turbulence grid used in this study, $\sigma \approx 0.5$, T^2 is 1250 cm^2, and P is 1175 cm, yielding $M_{\text{eff}} = 3$ cm. The thickness ratio, t_r, is the ratio of the maximum to minimum bar thickness, $t_{\max}/t_{\min}$; in our case $t_{\max} = 1.75$ cm, $t_{\min} = 0.6$ cm, and $t_r = 2.9$.

A key design feature of fractal turbulence grids is their ability to induce higher turbulence intensities relative to classical grids at the same flow velocity, but they do so at the cost of higher development lengths (defined as the downstream distance to peak turbulent kinetic energy) (Hurst and Vassilicos 2007). To characterize fractal grid behavior, Mazellier and Vassilicos (2010) identified a key quantity: the wake interaction length scale $x_\star$, which demarcates the regions of growth and decay of turbulence intensity as approximately $0.4x_\star$ (Vassilicos 2015) and to which the evolution of velocity statistics is proportional. The wake interaction length scale is computed as $x_\star = L_0^2/t_0$, where L_0 and t_0 are the side length and bar thickness, respectively, of the largest fractal iteration (in our case 16 cm and 1.75 cm), resulting in $x_\star$ =1.5 m for our fractal grid and an expected peak in turbulence intensity at 0.6 m. This is in contrast to the expected peak distance in our regular grid estimated as $4M$, where M is our mesh size (0.0254 m), resulting in an expected peak turbulence intensity at 0.1 m (Vassilicos 2015). However, to complicate matters, the low Reynolds number of our flow likely results in 'peculiar' behavior that does not strictly adhere to the aforementioned grid turbulence characterizations for high-Re flows (Duong and Tavoularis 2024). Of interest in our odor plume context, the differing flow fields generated from each of these grid types then has implications for passive scalar mixing downstream (Nedić and Tavoularis 2016; Suzuki et al. 2010).

We now quantify the turbulent kinetic energy and its dissipation rate in the velocity field for each of the cases presented in the main text. We begin with a Reynold's decomposition of the velocity field to isolate the temporal fluctuations (denoted using a prime) of each component of the velocity field at each time t as: $u'_t = u_t - \overline{u}$. Using these fluctuating velocity components, we compute the turbulent kinetic energy (TKE), which quantifies the energy in the fluctuating flow at each location as half the sum of mean square fluctuations:

$$TKE = \frac{1}{2}(\overline{u'^2} + \overline{v'^2} + \overline{w'^2}). \tag{E3}$$

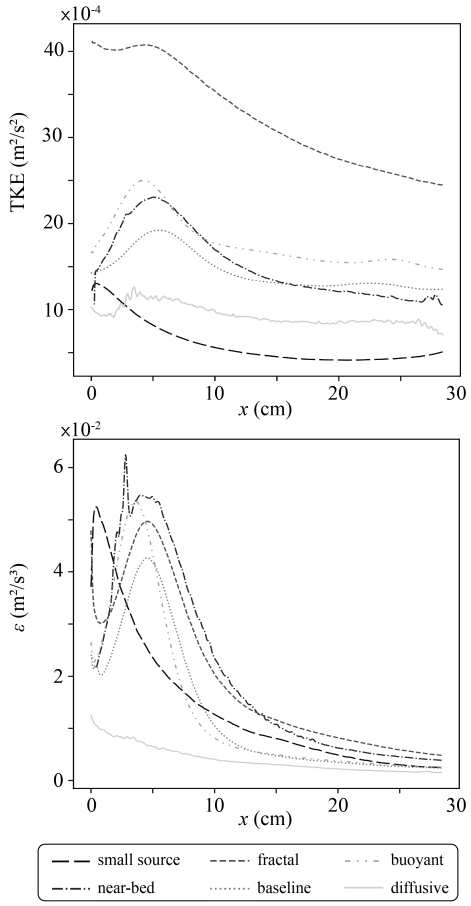


Fig. E5 Streamwise evolution of turbulence kinetic energy (TKE) and TKE dissipation rate (ϵ) for each plume configuration case, averaged cross-stream.

We then compute the fluctuating velocity gradient tensor with elements $\partial u_i'/\partial x_j$, which can be decomposed into its symmetric and antisymmetric parts. The symmetric component is the rate-of-strain tensor s_{ij}:

$$s_{ij} \equiv \frac{1}{2}\left(\frac{\partial u_i'}{\partial x_j} + \frac{\partial u_j'}{\partial x_i}\right), \tag{E4}$$

which allows us to compute the dissipation rate of turbulent kinetic energy, ϵ, as:

$$\epsilon = 2\nu\overline{s_{ij}s_{ij}}. \tag{E5}$$

We then approximate the dissipation rate with isotropy assumptions using:

$$\epsilon = 5\nu \left[\overline{\left(\frac{\partial u'}{\partial x}\right)^2} + \overline{\left(\frac{\partial v'}{\partial y}\right)^2} + \overline{\left(\frac{\partial w'}{\partial z}\right)^2} \right]. \tag{E6}$$

Note that two of the velocity gradient components, $\frac{\partial u'}{\partial x}$ and $\frac{\partial v'}{\partial y}$, are measured from our stereo PIV data, which then allows us to solve for $\frac{\partial w'}{\partial z}$ by continuity.

For plotting the streamwise evolution of these quantities, we average across the cross-stream direction to yield a single value at each streamwise position. As shown in Fig. E5, the TKE, and correspondingly the dissipation rate ϵ, peak a short distance downstream of the grid and decay from there to the end of the domain, as is characteristic of grid turbulence. As expected, the fractal grid induces a greater overall level of turbulent kinetic energy across the domain. Note, however, that these quantities also reflect the wake effects from the source tube, so are not strictly representing the grid turbulence in isolation.

We also quantify the key length scales in the velocity field for each case: at the smaller side of the spectrum, the Kolmogorov and Taylor microscales, and at the larger end, the integral length scales. The previously computed TKE dissipation rate enables the calculation of the Kolmogorov length scale as

$$\eta = \left(\frac{\nu^3}{\epsilon}\right)^{1/4} \tag{E7}$$

and the Taylor microscale as

$$\lambda = \sqrt{\frac{15\nu\overline{u'^2}}{\epsilon}}. \tag{E8}$$

Note that in our conditions of Sc≈1, the Batchelor length scale, λ_B, of the concentration field approximately follows the Kolmogorov length scale of the velocity field, since $\lambda_B = \eta/\sqrt{\mathrm{Sc}}$.

At the larger side of the spectrum, the integral scales represent the size of the most energy-containing eddies in the flow. Here we focus on the streamwise (x-direction) component of the velocity fluctuations due to the relatively low values of the cross-stream fluctuations. We compute the integral length scale (L_u) at each location using the spatial autocorrelation function (ACF) of the velocity field. For example, we computed the ACF of the streamwise velocity field in the y-direction by averaging the ACFs for positive and negative spatial displacements, r, as shown:

$$f_{u,y}(r;x,y) = \left(\frac{\overline{u(t;x,y)u(t;x,y+r)}}{\overline{u(t;x,y)u(t;x,y)}} + \frac{\overline{u(t;x,y)u(t;x,y-r)}}{\overline{u(t;x,y)u(t;x,y)}} \right)/2. \tag{E9}$$

Due to similar values of the ACF in the cross-stream and streamwise directions, we averaged $f_{u,y}$ and $f_{u,x}$ to obtain a single value f_u at each location. To arrive at the integral scale, we then integrate the autocorrelation function from 0 to the index of the first zero crossing, N_{cross}. For our discrete data, we compute this as

$$L_u = \sum_{n=0}^{N_{\text{cross}}} f_u(n\Delta r; x, y)\Delta r. \tag{E10}$$

For plotting the streamwise evolution of the length scales, we again average across the cross-stream direction to obtain the value at each downstream position. As shown in Fig. E6, nearly all characteristic length scales grow in the downstream direction due to the growth of turbulent eddies with distance from the grid due to the viscous dissipation of TKE with distance from the grid at the smallest scales of the flow (Isaza et al. 2014). The notable exception is the decrease of the integral length scale for the fractal grid case. While the shape of this fractal grid curve doesn't precisely mimic the trends in integral scales identified by (Hurst and Vassilicos 2007), they did observe an initial sharp decrease in initial integral scale prior to arriving at a relatively constant value. The dissimilar aspects of the integral scale curve in the current study likely arise from the atypical rectangular design of our fractal grid (as opposed to the typical square-shaped design), which introduces variations in the flow dynamics. Additionally, these length scales combine the effects of the grid turbulence and source wake into a single value via the cross-stream averaging, and so are not directly reflecting the grid turbulence in isolation.

References

Ackels T, Erskine A, Dasgupta D, et al (2021) Fast odour dynamics are encoded in the olfactory system and guide behaviour. Nature 593(7860):558–563. https://doi.org/10.1038/s41586-021-03514-2, URL https://www.nature.com/articles/s41586-021-03514-2

Bara B, Wilson D, Zelt B (1992) Concentration fluctuation profiles from a water channel simulation of a ground-level release. Atmospheric Environment Part A General Topics 26(6):1053–1062. https://doi.org/10.1016/0960-1686(92)90037-L, URL https://linkinghub.elsevier.com/retrieve/pii/096016869290037L

Boie SD, Connor EG, McHugh M, et al (2018) Information-theoretic analysis of realistic odor plumes: What cues are useful for determining location? PLOS Computational Biology 14(7):e1006275. https://doi.org/10.1371/journal.pcbi.1006275, URL https://dx.plos.org/10.1371/journal.pcbi.1006275

Cassiani M, Bertagni MB, Marro M, et al (2020) Concentration Fluctuations from Localized Atmospheric Releases. Boundary-Layer Meteorology 177(2-3):461–510. https://doi.org/10.1007/s10546-020-00547-4, URL https://link.springer.com/10.1007/s10546-020-00547-4

Celani A, Villermaux E, Vergassola M (2014) Odor Landscapes in Turbulent Environments. Physical Review X 4(4):041015. https://doi.org/10.1103/PhysRevX.4.041015, URL https://link.aps.org/doi/10.1103/PhysRevX.4.041015

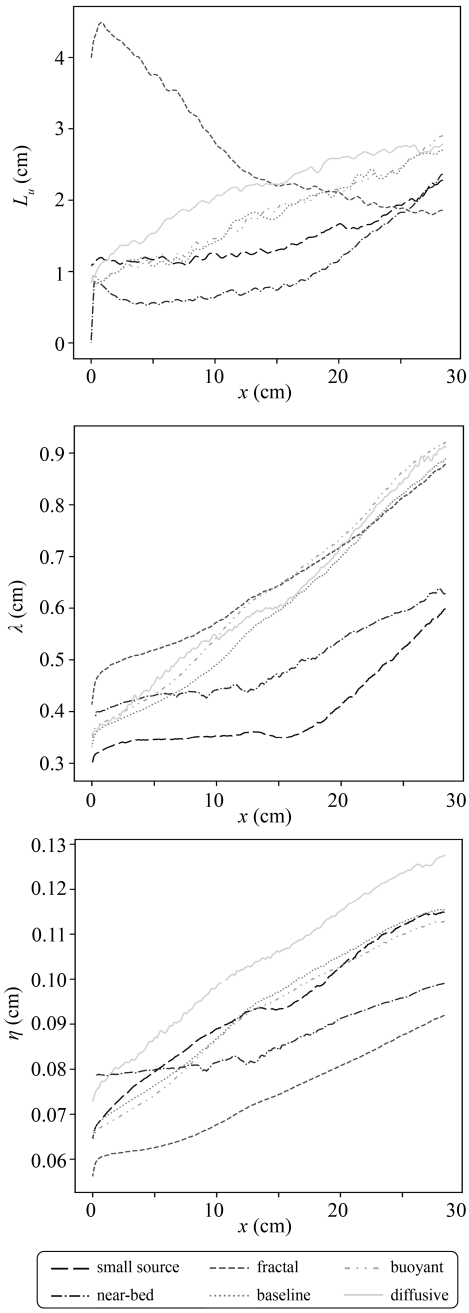


Fig. E6 Streamwise evolution of the Kolmogorov microscale (equivalent to the Batchelor scale since Sc=1), Taylor microscale, and integral length scale for each plume configuration case, averaged cross-stream.

Connor EG, McHugh MK, Crimaldi JP (2018) Quantification of airborne odor plumes using planar laser-induced fluorescence. Experiments in Fluids 59(9):137. https://doi.org/10.1007/s00348-018-2591-3, URL http://link.springer.com/10.1007/s00348-018-2591-3

Coriton B, Steinberg AM, Frank JH (2014) High-speed tomographic PIV and OH PLIF measurements in turbulent reactive flows. Experiments in Fluids 55(6):1743. https://doi.org/10.1007/s00348-014-1743-3, URL http://link.springer.com/10.1007/s00348-014-1743-3

Crimaldi J, Lei H, Schaefer A, et al (2022) Active sensing in a dynamic olfactory world. Journal of Computational Neuroscience 50(1):1–6. https://doi.org/10.1007/s10827-021-00798-1, URL https://link.springer.com/10.1007/s10827-021-00798-1

Crimaldi JP (2008) Planar laser induced fluorescence in aqueous flows. Experiments in Fluids 44(6):851–863. https://doi.org/10.1007/s00348-008-0496-2, URL http://link.springer.com/10.1007/s00348-008-0496-2, number: 6

Crimaldi JP, Koseff JR (2001) High-resolution measurements of the spatial and temporal scalar structure of a turbulent plume. Experiments in Fluids 31(1):90–102. https://doi.org/10.1007/s003480000263, URL http://link.springer.com/10.1007/s003480000263

Duong D, Tavoularis S (2024) Grid-generated velocity fields at very small Reynolds numbers. Physical Review Fluids 9(2):024607. https://doi.org/10.1103/PhysRevFluids.9.024607, URL https://link.aps.org/doi/10.1103/PhysRevFluids.9.024607, number: 2 Publisher: American Physical Society

Duplat J, Villermaux E (2008) Mixing by random stirring in confined mixtures. Journal of Fluid Mechanics 617:51–86. https://doi.org/10.1017/S0022112008003789, URL https://www.cambridge.org/core/product/identifier/S0022112008003789/type/journal_article

Dürr V, Berendes V, Strube-Bloss M (2022) Sensorimotor ecology of the insect antenna: Active sampling by a multimodal sensory organ. In: Advances in Insect Physiology, vol 63. Elsevier, p 1–105, https://doi.org/10.1016/bs.aiip.2022.10.002, URL https://linkinghub.elsevier.com/retrieve/pii/S0065280622000182

Filatyev S, Thariyan M, Lucht R, et al (2007) Simultaneous stereo particle image velocimetry and double-pulsed planar laser-induced fluorescence of turbulent premixed flames. Combustion and Flame 150(3):201–209. https://doi.org/10.1016/j.combustflame.2007.02.005, URL https://linkinghub.elsevier.com/retrieve/pii/S0010218007000569

Frank JH, Kalt PA, Bilger RW (1999) Measurements of conditional velocities in turbulent premixed flames by simultaneous OH PLIF and PIV. Combustion and Flame 116(1-2):220–232. https://doi.org/10.1016/S0010-2180(98)00041-8, URL https://

linkinghub.elsevier.com/retrieve/pii/S0010218098000418

Gifford F (1959) Statistical Properties of A Fluctuating Plume Dispersion Model. In: Advances in Geophysics, vol 6. Elsevier, p 117–137, https://doi.org/10.1016/S0065-2687(08)60099-0, URL https://linkinghub.elsevier.com/retrieve/pii/S0065268708600990

Gotoh T, Yeung P (2012) Passive Scalar Transport in Turbulence: A Computational Perspective, Cambridge University Press, p 87–131

Gumaste A, Coronas-Samano G, Hengenius J, et al (2020) A Comparison between Mouse, *In Silico* , and Robot Odor Plume Navigation Reveals Advantages of Mouse Odor Tracking. eneuro 7(1):ENEURO.0212–19.2019. https://doi.org/10.1523/ENEURO.0212-19.2019, URL https://www.eneuro.org/lookup/doi/10.1523/ENEURO.0212-19.2019

Gumaste A, Baker KL, Izydorczak M, et al (2024) Behavioral discrimination and olfactory bulb encoding of odor plume intermittency. eLife 13:e85303. https://doi.org/10.7554/eLife.85303, URL https://elifesciences.org/articles/85303

Haller G (2014) Lagrangian Coherent Structures. Annual Review of Fluid Mechanics https://doi.org/10.1146/annurev-fluid-010313-141322

Hengenius JB, Connor EG, Crimaldi JP, et al (2021) Olfactory navigation in the real world: Simple local search strategies for turbulent environments. Journal of Theoretical Biology 516:110607. https://doi.org/10.1016/j.jtbi.2021.110607, URL https://linkinghub.elsevier.com/retrieve/pii/S0022519321000291

Hurst D, Vassilicos JC (2007) Scalings and decay of fractal-generated turbulence. Physics of Fluids 19(3):035103. https://doi.org/10.1063/1.2676448, URL https://pubs.aip.org/pof/article/19/3/035103/255915/Scalings-and-decay-of-fractal-generated-turbulence

Isaza JC, Salazar R, Warhaft Z (2014) On grid-generated turbulence in the near- and far field regions. Journal of Fluid Mechanics 753:402–426. https://doi.org/10.1017/jfm.2014.375, URL https://www.cambridge.org/core/journals/journal-of-fluid-mechanics/article/on-gridgenerated-turbulence-in-the-near-and-far-field-regions/3DF69B27B72C17A1998186C0EF55A485

Jones FE (1978) The air density equation and the transfer of the mass unit. Journal of Research of the National Bureau of Standards 83(5)

Justus KA, Murlis J, Jones C, et al (2002) Measurement of Odor-Plume Structure in a Wind Tunnel Using a Photoionization Detector and a Tracer Gas. Environmental Fluid Mechanics 2(1/2):115–142. https://doi.org/10.1023/A:1016227601019, URL http://link.springer.com/10.1023/A:1016227601019

Kadakia N, Demir M, Michaelis BT, et al (2022) Odour motion sensing enhances navigation of complex plumes. Nature 611(7937):754–761. https://doi.org/10.1038/s41586-022-05423-4, URL https://www.nature.com/articles/s41586-022-05423-4

Kathman ND, Lanz AJ, Freed JD, et al (2024) Neural dynamics for working memory and evidence integration during olfactory navigation in *Drosophila*. https://doi.org/10.1101/2024.10.05.616803, URL http://biorxiv.org/lookup/doi/10.1101/2024.10.05.616803

Knutson B, Tang W, Chan PW (2015) Lagrangian Coherent Structure Analysis of Terminal Winds: Three-Dimensionality, Intramodel Variations, and Flight Analyses. Advances in Meteorology 2015:1–13. https://doi.org/10.1155/2015/816727, URL http://www.hindawi.com/journals/amete/2015/816727/

Liao Q, Cowen EA (2002) The Information Content of a Scalar Plume – A Plume Tracing Perspective. Environmental Fluid Mechanics https://doi.org/10.1023/A:1016231701928

Lim H, Vanderwel C (2023) Turbulent dispersion of a passive scalar in a smooth-wall turbulent boundary layer. Journal of Fluid Mechanics 969:A26. https://doi.org/10.1017/jfm.2023.562, URL https://www.cambridge.org/core/product/identifier/S0022112023005621/type/journal_article

Linstrom P (1997) NIST Chemistry WebBook, NIST Standard Reference Database 69. https://doi.org/10.18434/T4D303, URL http://webbook.nist.gov/chemistry/

Lozano A, Yip B, Hanson RK (1992) Acetone: a tracer for concentration measurements in gaseous flows by planar laser-induced fluorescence. Experiments in Fluids 13(6):369–376. https://doi.org/10.1007/BF00223244, URL http://link.springer.com/10.1007/BF00223244

Mazellier N, Vassilicos JC (2010) Turbulence without Richardson–Kolmogorov cascade. Physics of Fluids 22(7):075101. https://doi.org/10.1063/1.3453708, URL https://pubs.aip.org/pof/article/22/7/075101/256560/Turbulence-without-Richardson-Kolmogorov-cascade

Moore PA, Atema J (1991) Spatial Information in the Three-Dimensional Fine Structure of an Aquatic Odor Plume. The Biological Bulletin 181(3):408–418. https://doi.org/10.2307/1542361, URL https://www.journals.uchicago.edu/doi/10.2307/1542361

Murlis J, Elkinton JS, Cardé RT (1992) Odor Plumes and How Insects Use Them. Annual Review of Entomology 37(1):505–532. https://doi.org/10.1146/annurev.en.37.010192.002445, URL https://www.annualreviews.org/doi/10.1146/annurev.en.37.010192.002445

Murlis J, Willis MA, Cardé RT (2000) Spatial and temporal structures of pheromone plumes in fields and forests. Physiological Entomology 25(3):211–222. https://doi.org/10.1046/j.1365-3032.2000.00176.x, URL https://resjournals.onlinelibrary.wiley.com/doi/10.1046/j.1365-3032.2000.00176.x

Nag A, Van Breugel F (2024) Odour source distance is predictable from a time history of odour statistics for large scale outdoor plumes. Journal of The Royal Society Interface 21(216):20240169. https://doi.org/10.1098/rsif.2024.0169, URL https://royalsocietypublishing.org/doi/10.1098/rsif.2024.0169

Nedić J, Tavoularis S (2016) Measurements of passive scalar diffusion downstream of regular and fractal grids. Journal of Fluid Mechanics 800:358–386. https://doi.org/10.1017/jfm.2016.385, URL https://www.cambridge.org/core/product/identifier/S0022112016003852/type/journal_article

Nironi C, Salizzoni P, Marro M, et al (2015) Dispersion of a Passive Scalar Fluctuating Plume in a Turbulent Boundary Layer. Part I: Velocity and Concentration Measurements. Boundary-Layer Meteorology 156(3):415–446. https://doi.org/10.1007/s10546-015-0040-x, URL http://link.springer.com/10.1007/s10546-015-0040-x

Patel M, Kulkarni N, Lei HH, et al (2022) Experimental and theoretical probe on mechano- and chemosensory integration in the insect antennal lobe. Frontiers in Physiology 13:1004124. https://doi.org/10.3389/fphys.2022.1004124, URL https://www.frontiersin.org/articles/10.3389/fphys.2022.1004124/full

Peacock T, Haller G (2013) Lagrangian coherent structures: The hidden skeleton of fluid flows. Physics Today 66(2):41–47. https://doi.org/10.1063/PT.3.1886, URL https://pubs.aip.org/physicstoday/article/66/2/41/414328/Lagrangian-coherent-structures-The-hidden-skeleton

Petersson P, Olofsson J, Brackman C, et al (2007) Simultaneous PIV/OH-PLIF, Rayleigh thermometry/OH-PLIF and stereo PIV measurements in a low-swirl flame. Applied Optics 46(19):3928. https://doi.org/10.1364/AO.46.003928, URL https://opg.optica.org/ao/abstract.cfm?uri=ao-46-19-3928

Prasad AK (2000) Stereoscopic particle image velocimetry. Experiments in Fluids 29(2):103–116. https://doi.org/10.1007/s003480000143, URL http://link.springer.com/10.1007/s003480000143

Rahman S, Webster DR (2005) The effect of bed roughness on scalar fluctuations in turbulent boundary layers. Experiments in Fluids 38(3):372–384. https://doi.org/10.1007/s00348-004-0919-7, URL http://link.springer.com/10.1007/s00348-004-0919-7

Reddy G, Murthy VN, Vergassola M (2022) Olfactory Sensing and Navigation in Turbulent Environments. Annual Review of Condensed Matter Physics 13(1):191–213. https://doi.org/10.1146/annurev-conmatphys-031720-032754, URL https://www.

annualreviews.org/doi/10.1146/annurev-conmatphys-031720-032754

Reijtenbagh J, Westerweel J, Van De Water W (2021) Large-scale structures of scalar and velocity in a turbulent jet flow. 14th International Symposium on Particle Image Velocimetry 1(1). https://doi.org/10.18409/ispiv.v1i1.28, URL https://ispiv21.library.iit.edu/index.php/ISPIV/article/view/28

Rogers MM, Mansour NN, Reynolds WC (1989) An algebraic model for the turbulent flux of a passive scalar. Journal of Fluid Mechanics 203:77–101. https://doi.org/10.1017/S0022112089001382, URL https://www.cambridge.org/core/product/identifier/S0022112089001382/type/journal_article

Sadanandan R, Stöhr M, Meier W (2008) Simultaneous OH-PLIF and PIV measurements in a gas turbine model combustor. Applied Physics B 90(3-4):609–618. https://doi.org/10.1007/s00340-007-2928-8, URL http://link.springer.com/10.1007/s00340-007-2928-8

Álvarez Salvado E, Licata AM, Connor EG, et al (2018) Elementary sensory-motor transformations underlying olfactory navigation in walking fruit-flies. eLife 7:e37815. https://doi.org/10.7554/eLife.37815, URL https://elifesciences.org/articles/37815

Schumacher J, Scheel JD, Krasnov D, et al (2014) Small-scale universality in fluid turbulence. Proceedings of the National Academy of Sciences 111(30):10961–10965. https://doi.org/10.1073/pnas.1410791111, URL https://pnas.org/doi/full/10.1073/pnas.1410791111

Shadden SC, Lekien F, Marsden JE (2005) Definition and properties of Lagrangian coherent structures from finite-time Lyapunov exponents in two-dimensional aperiodic flows. Physica D: Nonlinear Phenomena 212(3-4):271–304. https://doi.org/10.1016/j.physd.2005.10.007, URL https://linkinghub.elsevier.com/retrieve/pii/S0167278905004446

Sharaborin DK, Savitskii AG, Bakharev GY, et al (2021) PIV/PLIF investigation of unsteady turbulent flow and mixing behind a model gas turbine combustor. Experiments in Fluids 62(5):96. https://doi.org/10.1007/s00348-021-03181-z, URL https://link.springer.com/10.1007/s00348-021-03181-z

Siliciano AF, Minni S, Morton C, et al (2025) A vector-based strategy for olfactory navigation in *Drosophila*. https://doi.org/10.1101/2025.02.15.638426, URL http://biorxiv.org/lookup/doi/10.1101/2025.02.15.638426

Simoens S, Ayrault M (1994) Concentration flux measurements of a scalar quantity in turbulent flows. Experiments in Fluids 16-16(3-4):273–281. https://doi.org/10.1007/BF00206547, URL http://link.springer.com/10.1007/BF00206547

Smith BL, Neal DR (2016) Particle Image Velocimetry. In: Handbook of Fluid Dynamics, 2nd edn. Taylor & Francis Group

Speetjens M, Metcalfe G, Rudman M (2021) Lagrangian Transport and Chaotic Advection in Three-Dimensional Laminar Flows. Applied Mechanics Reviews 73(3):030801. https://doi.org/10.1115/1.4050701, URL https://asmedigitalcollection.asme.org/appliedmechanicsreviews/article/73/3/030801/1106104/Lagrangian-Transport-and-Chaotic-Advection-in

Sreenivasan KR (2019) Turbulent mixing: A perspective. Proceedings of the National Academy of Sciences 116(37):18175–18183. https://doi.org/10.1073/pnas.1800463115, URL https://pnas.org/doi/full/10.1073/pnas.1800463115

Steele TJ, Lanz AJ, Nagel KI (2023) Olfactory navigation in arthropods. Journal of Comparative Physiology A 209(4):467–488. https://doi.org/10.1007/s00359-022-01611-9, URL https://link.springer.com/10.1007/s00359-022-01611-9

Stupski SD, Van Breugel F (2024) Wind gates olfaction-driven search states in free flight. Current Biology 34(19):4397–4411.e6. https://doi.org/10.1016/j.cub.2024.07.009, URL https://linkinghub.elsevier.com/retrieve/pii/S0960982224009126

Sulman MH, Huntley HS, Lipphardt B, et al (2013) Leaving flatland: Diagnostics for Lagrangian coherent structures in three-dimensional flows. Physica D: Nonlinear Phenomena 258:77–92. https://doi.org/10.1016/j.physd.2013.05.005, URL https://linkinghub.elsevier.com/retrieve/pii/S0167278913001450

Suver MP, Medina AM, Nagel KI (2023) Active antennal movements in Drosophila can tune wind encoding. Current Biology 33(4):780–789.e4. https://doi.org/10.1016/j.cub.2023.01.020, URL https://linkinghub.elsevier.com/retrieve/pii/S0960982223000209

Suzuki H, Nagata K, Sakai Y, et al (2010) High-Schmidt-number scalar transfer in regular and fractal grid turbulence. Physica Scripta T142:014069. https://doi.org/10.1088/0031-8949/2010/T142/014069, URL https://iopscience.iop.org/article/10.1088/0031-8949/2010/T142/014069

Szyszka P, Gerkin RC, Galizia CG, et al (2014) High-speed odor transduction and pulse tracking by insect olfactory receptor neurons. Proceedings of the National Academy of Sciences 111(47):16925–16930. https://doi.org/10.1073/pnas.1412051111, URL https://pnas.org/doi/full/10.1073/pnas.1412051111

Tanahashi M, Murakami S, Choi GM, et al (2005) Simultaneous CH–OH PLIF and stereoscopic PIV measurements of turbulent premixed flames. Proceedings of the Combustion Institute 30(1):1665–1672. https://doi.org/10.1016/j.proci.2004.08.270, URL https://linkinghub.elsevier.com/retrieve/pii/S0082078404003248

Tiraboschi E, Leonardelli L, Segata G, et al (2021) Parallel Processing of Olfactory and Mechanosensory Information in the Honey Bee Antennal Lobe. Frontiers in Physiology 12:790453. https://doi.org/10.3389/fphys.2021.790453, URL https://www.frontiersin.org/articles/10.3389/fphys.2021.790453/full

Tuckman H, Kim J, Rangan A, et al (2021) Dynamics of sensory integration of olfactory and mechanical stimuli within the response patterns of moth antennal lobe neurons. Journal of Theoretical Biology 509:110510. https://doi.org/10.1016/j.jtbi.2020.110510, URL https://linkinghub.elsevier.com/retrieve/pii/S0022519320303659

Tung YC, Shih YC, Hu SC (2009) Numerical study on the dispersion of airborne contaminants from an isolation room in the case of door opening. Applied Thermal Engineering 29(8-9):1544–1551. https://doi.org/10.1016/j.applthermaleng.2008.07.009, URL https://linkinghub.elsevier.com/retrieve/pii/S1359431108003050

Van Cruyningen I, Lozano A, Hanson RK (1990) Quantitative imaging of concentration by planar laser-induced fluorescence. Experiments in Fluids 10(1):41–49. https://doi.org/10.1007/BF00187871, URL http://link.springer.com/10.1007/BF00187871

Vassilicos JC (2015) Dissipation in Turbulent Flows. Annual Review of Fluid Mechanics 47(1):95–114. https://doi.org/10.1146/annurev-fluid-010814-014637, URL https://www.annualreviews.org/doi/10.1146/annurev-fluid-010814-014637

Victor JD, Boie SD, Connor EG, et al (2019) Olfactory Navigation and the Receptor Nonlinearity. The Journal of Neuroscience 39(19):3713–3727. https://doi.org/10.1523/JNEUROSCI.2512-18.2019, URL https://www.jneurosci.org/lookup/doi/10.1523/JNEUROSCI.2512-18.2019

Wall IE, Pathikonda G (2025) Coherent organisation of passive scalar from a point source in a turbulent boundary layer. Journal of Fluid Mechanics 1025:A8. https://doi.org/10.1017/jfm.2025.10926, URL https://www.cambridge.org/core/product/identifier/S0022112025109269/type/journal_article

Warhaft Z (2000) Passive Scalars in Turbulent Flows. Annual Review of Fluid Mechanics 32(1):203–240. https://doi.org/10.1146/annurev.fluid.32.1.203, URL https://www.annualreviews.org/doi/10.1146/annurev.fluid.32.1.203

Webster DR, Weissburg MJ (2001) Chemosensory guidance cues in a turbulent chemical odor plume. Limnology and Oceanography 46(5):1034–1047. https://doi.org/10.4319/lo.2001.46.5.1034, URL https://aslopubs.onlinelibrary.wiley.com/doi/10.4319/lo.2001.46.5.1034

Wieneke B (2005) Stereo-PIV using self-calibration on particle images. Experiments in Fluids 39(2):267–280. https://doi.org/10.1007/s00348-005-0962-z, URL https://doi.org/10.1007/s00348-005-0962-z, number: 2

Wilson D, Robins A, Fackrell J (1985) Intermittency and conditionally-averaged concentration fluctuation statistics in plumes. Atmospheric Environment (1967) 19(7):1053–1064. https://doi.org/10.1016/0004-6981(85)90189-1, URL https://linkinghub.elsevier.com/retrieve/pii/0004698185901891

Yee E, Skvortsov A (2011) Scalar fluctuations from a point source in a turbulent boundary layer. Physical Review E 84(3):036306. https://doi.org/10.1103/PhysRevE.84.036306, URL https://link.aps.org/doi/10.1103/PhysRevE.84.036306

Young DL, Webster DR, Larsson AI (2022) Structure and mixing of a meandering turbulent chemical plume: turbulent mixing and eddy diffusivity. Experiments in Fluids 63(1):3. https://doi.org/10.1007/s00348-021-03354-w, URL https://link.springer.com/10.1007/s00348-021-03354-w